Retroviral Infection of Human Neurospheres and Use of Stem Cell EVs to Repair Cellular Damage

Heather Branscome[1, 2], Pooja Khatkar[1], Sarah Al Sharif[1], Dezhong Yin[3], Sheela Jacob[3], Maria Cowen[1], Yuriy Kim[1], James Erickson[1], Christine A. Brantner[4], Nazira El-Hage[5], Lance A. Liotta[6] and Fatah Kashanchi[1*]

[1] Laboratory of Molecular Virology, School of Systems Biology, George Mason University, Manassas, VA.

[2] American Type Culture Collection (ATCC), Manassas, VA.

[3]ATCC Cell Systems, Gaithersburg, MD.

[4] GW Nanofabrication and Imaging Center, George Washington University, Washington, DC.

[5]Department of Immunology and Nano-Medicine, Herbert Wertheim College of Medicine, Florida International University, Miami, FL.

[6]Center for Applied Proteomics and Molecular Medicine, George Mason University, Manassas, VA.

*** Correspondence:** Fatah Kashanchi, Ph.D., Laboratory of Molecular Virology, George Mason University, Discovery Hall Room 182, 10900 University Blvd., Manassas, VA 20110. Tel.: 703-993-9160, Fax: 703-993-7022. Email: fkashanc@gmu.edu

Abstract

HIV-1 remains an incurable infection that is associated with substantial economic and epidemiologic impacts. HIV-associated neurocognitive disorders (HAND) are commonly linked with HIV-1 infection; despite the development of combination antiretroviral therapy (cART), HAND is still reported to affect at least 50% of HIV-1 infected individuals. It is believed that the over-amplification of inflammatory pathways, along with release of toxic viral proteins from infected cells, are primarily responsible for the neurological damage that is observed in HAND; however, the underlying mechanisms are not well-defined. Therefore, there is an unmet need to develop more physiologically relevant and reliable platforms for studying these pathologies. In recent years, neurospheres derived from induced pluripotent stem cells (iPSCs) have been utilized to model the effects of different neurotropic viruses. Here, we report the generation of neurospheres from iPSC-derived neural progenitor cells (NPCs) and we show that these cultures are permissive to retroviral (e.g. HIV-1, HTLV-1) replication. In addition, we also examine the potential effects of stem cell derived extracellular vesicles (EVs) on HIV-1 damaged cells as there is abundant literature supporting the reparative and regenerative properties of stem cell EVs in the context of various CNS pathologies. Consistent with the literature, our data suggests that stem cell EVs may modulate neuroprotective and anti-inflammatory properties in damaged cells. Collectively, this study demonstrates the feasibility of NPC-derived neurospheres for modeling HIV-1 infection and, subsequently, highlights the potential of stem cell EVs for rescuing cellular damage induced by HIV-1 infection.

Keywords: Neurospheres, neural progenitor cells (NPCs), HIV-1, stem cells, extracellular vesicles (EVs)

54 **Introduction**

55 HIV-1 remains an incurable infection and as of 2018 approximately 37.9 million people were estimated to
56 be living with HIV-1, with an average of 1.7 million new infections occurring annually [1]. In addition to its
57 deleterious impact on the immune system, HIV-1 also contributes to neurocognitive impairments. HIV-associated
58 neurocognitive disorders (HAND) are commonly associated with HIV-1 infection and comprise a range of
59 neurological dysfunctions, including asymptomatic neurocognitive impairment, mild neurocognitive disorder, and
60 HIV-associated dementia [2]. Despite the development of combination antiretroviral therapy (cART), which
61 effectively suppresses viral replication and has vastly improved the quality of life for those treated, HAND is still
62 reported to affect up to 50% of infected individuals [3,4]. Therefore, HAND represents a considerable cause of
63 morbidity in these populations.

64 Although the exact mechanisms that contribute to its persistence are poorly understood, it is believed that
65 the over-amplification of inflammatory pathways, along with the release of toxic viral proteins from infected cells,
66 are primarily responsible for the neurological damage that is observed in HAND [5,6,7]. While neurons are not
67 directly infected by HIV-1, they remain highly susceptible to the cellular damage and injury mediated by viral
68 proteins such as gp120 and Tat [8]. Additionally, the release of pro-inflammatory cytokines, including TNF-α, IL-
69 1β and IL-6, from infected macrophages and microglia can also promote neuronal damage and neuronal apoptosis
70 and it has also been suggested that exposure of astrocytes to these factors can further exacerbate neurotoxic effects
71 [5,6]. Consequently, there is a gap of knowledge surrounding the neuropathology of HAND and the mechanisms
72 that contribute to its persistence.

73 The complexity of the Central Nervous System (CNS) relative to other systems in the body has largely
74 limited the progress of CNS disease modeling and drug development. Moreover, the global incidence of CNS
75 diseases, including neurocognitive and neurodegenerative disorders as well as neurological infections, has
76 substantially risen throughout the last several decades. This, in turn, imposes a substantial socioeconomic burden.
77 For example, a recent report found that approximately 16.5% of global deaths are caused by neurological diseases
78 and the estimated costs associated with these diseases are expected to range from $600 to $700 million [9, 10]. This
79 underscores the outstanding need for the development of novel research platforms which can allow for improved
80 modeling of CNS pathologies, including those related to HIV-1 infection.

81 Improvements in biotechnology, coupled with progress in stem cell research, have revolutionized the

82 biomedical field during the last decade. Specifically, induced pluripotent stem cells (iPSCs) represent a relatively
83 novel platform that has allowed for advanced disease modeling and drug discovery [11]. Using this technology,
84 adult somatic cells can be reprogrammed into an embryonic-like state via the overexpression of transcription factors
85 (e.g. Oct3/4, SOX2, c-Myc, Klf4) responsible for maintaining pluripotency. Takahashi and Yamanaka first
86 demonstrated this in 2006 with the successful reprogramming of mouse somatic cells into iPSCs and again, in 2007,
87 when they generated iPSCs from human fibroblasts [12, 13]. In the context of the CNS, iPSCs have the potential to
88 differentiate into a wide variety of neuronal and glial cell types including dopaminergic, cortical, and motor neurons
89 as well as astrocytes, oligodendrocytes, microglia, and neural precursors [14, 15, 16, 17]. Along these lines, iPSCs
90 have been employed to model a number of different CNS pathologies ranging from Alzheimer's, Parkinson's, and
91 Huntington's disease, to amyotrophic lateral sclerosis, multiple system atrophy, and Zika, West Nile virus, and HIV-
92 1 [18, 19, 20, 21, 22, 23, 24, 25].

93 In recent years, human iPSCs have been used to derive neural stem cells (NSCs) and/or neural progenitor
94 cells (NPCs); these neuronal cultures have subsequently been used to efficiently generate three-dimensional (3D)
95 neurospheres *in vitro*. In general, 3D models are expected to be superior to traditional 2D culture models of NPCs
96 due to their resemblance to the *in vivo* cellular environment which permits a more accurate representation of tissue-
97 specific architecture and cell to cell communication [26, 27, 28]. Along these lines, it has been demonstrated that
98 NPC-derived neurospheres are similar to those derived from primary fetal human NPCs with respect to migration,
99 proliferation, and differentiation [29]. Additionally, it has previously been shown that neurospheres partially
100 maintain regionally specific expression of developmental control genes *in vitro* and, moreover, that cells derived
101 from these spheres retain the ability to differentiate into cellular subtypes representative of their regional origin [30,
102 31, 32]. Therefore, the use of 3D neurospheres is expected to serve as a complementary approach to *in vivo* studies
103 relating to neurogenesis and neural development.

104 More recently, others have employed the use of 3D neurospheres to model the effects of different
105 neurotropic viruses. For example, Garcez et al. investigated the consequences of Zika virus (ZIKV) infection and
106 found that human iPSC-derived neurospheres exposed to ZIKV exhibited morphological abnormalities and had a
107 higher induction of apoptosis relative to mock infection [33]. In a follow-up study which included proteomic and
108 mRNA transcriptional profiling of infected neurospheres, these authors generated further data suggesting that ZIKV
109 impaired pathways related to cell cycle and neuronal differentiation [34]. Additionally, D'Aiuto et al. utilized

110 human iPSCs to generate 3D neurospheres to evaluate herpes simplex virus type 1 (HSV-1) infection [35]. The
111 results from these studies demonstrated that neurospheres remained viable after four weeks in culture, were capable
112 of differentiating into not only mature neurons (glutamatergic, GABAergic, dopaminergic) but also glial cells, and
113 could be applied in a high throughput fashion for drug screening. It is also worth noting that while this manuscript
114 was in-process, Dos Reis et al. published a similar study that utilized NPC-derived 3D organoids co-cultured with
115 HIV-1 infected microglia. The results from these experiments not only confirmed the replication potential of HIV-1
116 in these cultures but were also consistent with the expected neurodegenerative and pro-inflammatory phenotypes
117 associated with HIV-1 infection [36]. Taken together, this research strongly suggests that neurospheres are
118 physiologically relevant models that can be used to study not only the cellular and molecular interactions in both
119 healthy and diseased states but can also serve as a reliable platform for drug testing. Furthermore, they set an
120 essential precedent for the modeling of other neurotropic viruses.

121 As described earlier, the development of CNS therapeutics has met relatively limited success. Factors
122 relating to overall disease complexity, lengthy developmental periods and stringent regulatory review, coupled with
123 the challenge of drug delivery across the blood-brain-barrier (BBB) have hindered progress in this field [37, 38].
124 While stem cell therapy has been studied in the context of CNS pathologies, there is now an emerging interest in the
125 potential therapeutic application of stem cell-derived extracellular vesicles (EVs) as these vesicles have been shown
126 to mediate many of the reparative and regenerative properties associated with their donor stem cells [39]. Briefly,
127 EVs are nano-sized vesicles that are generally classified by their size and biogenesis. Two of the most widely
128 studied subtypes of EVs are exosomes, which range approximately 50 to 150 nm in size and originate from the
129 endosomal pathway, and microvesicles (MVs), which range approximately 50 to 1000 nm in size and are released
130 directly from the plasma membrane [40]. EVs are enriched with a diverse array of biological cargo which includes
131 RNAs, proteins, cytokines, and lipids and this cargo is believed to drive their potent functional effects [41, 42].
132 Accordingly, EVs from both mesenchymal stem cells (MSCs) and iPSCs have been broadly studied for their
133 functional effects and there is rich literature to support their potential therapeutic application in various pathologies
134 as reviewed elsewhere [43, 44].

135 With respect to the CNS, there is accumulating evidence which strongly indicates that stem cell EVs exert
136 both immunomodulatory and neuroprotective effects to promote functional recovery in damaged tissue [45, 46, 47,
137 48]. However, it is important to note that this field is still in its infancy. Moreover, whether stem cell EVs may

138 confer beneficial effects in the context of CNS infection, including HIV-1 and HAND, remains to be addressed.
139 Thus, studies of this nature are imperative to better characterize the potential neuroprotective properties of stem cell
140 EVs and to determine the mechanisms by which these EVs may repair cellular damage that is induced by different
141 viral infections.

142 Here, we report the generation of neurospheres from NPCs derived from normal human iPSCs. These
143 cultures not only exhibit reproducibility with respect to morphology and size but also demonstrate the ability to be
144 stably maintained in culture to permit differentiation into different CNS cell types. Importantly, our data suggests
145 that these cultures are permissive to HIV-1 infection. Additionally, we include data to show that neurospheres co-
146 cultured with HTLV-1 infected cells may also be susceptible to HTLV-1 infection. Lastly, we evaluated the
147 potential reparative effects of both MSC and iPSC EVs on HIV-1 damaged cells in both 2D cultures and 3D
148 neurospheres. Collectively, this data highlights NPC-derived neurospheres as relevant and robust models for future
149 studies relating to HIV-1 infection and HAND and, subsequently, demonstrates the potential application of stem cell
150 EVs for rescuing cellular damage induced by HIV-1 infection.

151

152
153
154
155
156
157
158
159
160
161
162
163
164
165
166

167 **Results**

168 **Generation and Characterization of NPC-derived Neurospheres**

169 The ability of NPCs to aggregate and assemble into physiologically relevant 3D structures that are also
170 permissive to viral replication, including Zika, HSV-1, and more recently HIV-1, has been published by others [27,
171 33, 34, 35, 36, 49]. To further expand upon these studies, we sought to evaluate the susceptibility of NPC-derived
172 neurospheres to retroviral infection. For these studies we utilized commercially available NPCs that had been
173 established from normal human iPSCs. The diagram in Fig. 1a summarizes the overall workflow and timeline
174 associated with the generation of NPCs and neurospheres. Briefly, adult somatic cells were directly reprogrammed
175 into iPSCs using a non-integrating Sendai-based reprogramming kit following established protocols [50]. To
176 authenticate the quality of iPSCs, their germ line differentiation potential was confirmed by pluripotency testing
177 (PluriTest); furthermore, flow cytometry was performed to confirm the positive expression (>85%) of the
178 pluripotency stem cell markers SSEA4 and TRA-1-60. iPSCs then underwent embryoid body (EB) formation to
179 assemble into spherical colonies that were subsequently differentiated into NPCs. NPCs were briefly scaled up in
180 2D culture prior to the induction of neurosphere formation.

181 In an effort to promote the controlled and consistent formation of neurospheres, NPCs were seeded at a
182 high density in individual U-shaped wells of an ultra-low attachment 96-well plate. After 48 to 72 hours of
183 incubation a single, well-defined neurosphere was visible in each well. Representative phase contrast images in Fig.
184 1b show that this methodology resulted in uniformly shaped spheres that maintained their morphology and structure
185 throughout the two week differentiation process (weeks 12 through 14). Using calibrated imaging software, the
186 average diameter of each sphere in Fig. 1b was measured and graphed. As shown in Fig. 1c, the average diameter of
187 the neurospheres remained between 700 to 800 µm. This quantitative analysis indicates that NPC-derived
188 neurospheres maintain a relatively consistent size over time and, moreover, demonstrates the reproducibility of our
189 protocols.

190 As part of routine quality control testing, the NPCs used in these experiments were previously
191 characterized via immunocytochemistry (ICC), which confirmed positive expression of the NSC markers Nestin and
192 Pax6. Additionally, these NPCs have displayed robust expression of the early neuronal marker Tuj1, the
193 dopaminergic marker tyrosine hydroxylase (TH), and the astrocytic marker GFAP when cultured in the appropriate
194 differentiation medium (Supplementary Fig. 1a). This data is consistent with the reports of others who have shown

195 that NPCs are capable of differentiating into not only mature neurons but also glial cells [51, 52, 53, 54, 55]. Given
196 these results, we rationalized that NPC-derived neurospheres would retain their inherent differentiation capacity in
197 3D cultures.

198 Cross-sectioning and ICC staining of neurospheres that had been cultured in differentiation medium for two
199 weeks indicated that neurospheres were composed of a mixed population of cells which included NPCs ($SOX2^+$),
200 dopaminergic neurons (TH^+), astrocytes ($GFAP^+$), and microglia-like ($IBA\text{-}1^+$) cells. Representative images of
201 stained cross-sections (Fig. 1d) suggest that both NPCs and neurons are relatively diffuse and uniformly distributed
202 throughout the spheres. On the other hand, glial cells appeared to be more co-localized towards the periphery of the
203 spheres, as indicated by expression of GFAP and IBA-1. Additionally, H&E histological staining illustrated the
204 relatively compact and dense structure of cross-sectioned neurospheres (Supplementary Fig. 1b). Collectively, this
205 data highlights the ability of iPSC-derived NPCs to self-assemble into neurospheres that maintain their ability to
206 differentiate into both neurons and glial cells.

207 **Infection of Neurospheres**

208 To assess the susceptibility of NPC-derived neurospheres to HIV-1 infection, neurospheres were cultured
209 in the presence of HIV-1 dual tropic 89.6 (MOI:10). In addition, since HIV-1 infected individuals utilize combined
210 antiretroviral therapy (cART), neurospheres were also treated with a cocktail consisting of equal parts lamivudine,
211 tenofovir disoproxil fumarate, emtricitabine, and indinavir to model the effects of cART [1]. After a period of
212 fourteen days in culture, supernatants were collected and neurospheres were harvested for downstream assays. To
213 determine whether exposure of neurospheres to HIV-1 resulted in effective viral replication, total cellular protein
214 was isolated and western blot was performed to assess the expression of different viral proteins. As shown in Fig.
215 2a, uncleaved Gag polyprotein Pr55, p24 capsid protein, and accessory protein Nef were all detected in neurospheres
216 exposed to HIV-1 89.6.

217 The cART cocktail used for these experiments consisted of a mixture of nucleoside reverse transcriptase
218 inhibitors (NRTIs) and a protease inhibitor; as expected, culturing of HIV-1 neurospheres with cART reduced the
219 expression of Pr55, p24, and Nef to almost undetectable levels (Fig. 2a). RT-qPCR for HIV-1 TAR and *env*
220 confirmed the presence of these RNAs in HIV-1 89.6-exposed neurospheres with approximately 10^9 and 10^7 copies
221 being detected, respectively, relative to the control (uninfected) neurospheres (Fig. 2b). Treatment of HIV-1
222 neurospheres with cART decreased the expression of both TAR and *env* RNA relative to the HIV-1 sample, with a

223 significant reduction in the expression of TAR.

224 To validate these results, we also exposed neurospheres to two other HIV-1 lab adapted strains, JR-CSF
225 (MOI:10) and CHO40 (MOI:10) with or without cART. After seven days in culture, supernatants were collected
226 and neurospheres were harvested for downstream assays. Total cellular proteins were isolated and, again, western
227 blot showed the expression of p24 capsid protein in neurospheres that had been exposed to each viral isolate (Fig.
228 2c). Moreover, the level of p24 expression appeared relatively consistent among 89.6, JR-CSF, and CHO40-
229 exposed neurospheres. Collectively, this data shows that HIV-1 viral replication occurs in NPC-derived
230 neurospheres in a reproducible manner.

231 We were also interested in examining the potential tropism of HIV-1 in neurospheres. While $CD4^+$T cells
232 are the most abundantly HIV-1 infected cells in the body there is ample evidence to suggest that microglia and
233 astrocytes are not only capable of being infected by HIV-1, but may also serve as viral reservoirs, as reported
234 elsewhere [56, 57, 58, 59, 60, 61, 62]. For this experiment, NPCs were gently disaggregated with trypsin and
235 immunoprecipitation (IP) was performed using antibodies for either astrocytes ($GFAP^+$), microglia-like cells
236 ($CD11b^+$), mature neurons ($GAD65^+$), or NSCs ($SOX2^+$). We next performed direct PCR of the IP material without
237 purification of DNA, as RNA isolation from a relatively small number of infected cells would not yield a sufficient
238 amount of sample material for RT-qPCR. Results from qPCR confirmed the presence of TAR DNA in microglia-
239 like cells in the 89.6, JR-CSF, and CHO40 infected neurospheres (Fig. 2d). While the highest numbers of TAR
240 DNA were associated with astrocytes (~480 copies) and microglia-like cells (~780 copies) in the JR-CSF samples,
241 lower amounts were also detected in microglia-like cells from the 89.6 (~ 114 copies) and CHO40 (~ 125 copies)
242 samples. In addition, astrocytes from the JR-CSF neurospheres (~480 copies) had substantially higher levels of
243 TAR DNA than astrocytes from the 89.6 and CHO40-infected neurospheres (< 20 copies each). However, within
244 the JR-CSF samples, TAR DNA was still the most abundant in microglia-like cells. Consistent with the literature,
245 this data suggests that HIV-1 tropism in neurospheres is directed towards glial cells [56, 57, 58, 59, 60, 61, 62].

246 Based on this data, and given that microglia are the prominent innate immune cells in the CNS and,
247 therefore, represent a major target of HIV-1, we next attempted to increase the population of myeloid cells in
248 neurospheres to better assess the replication potential of HIV-1. To this end, differentiated neurospheres were
249 treated with the following cytokines: IL-34 (100 ng/mL), M-CSF (25 ng/mL), TGFβ-1 (50 ng/mL) every other day
250 for a period of seven days, as previous studies have demonstrated the ability of these cytokines to induce microglia

251 differentiation in iPSCs [16, 63, 64]. Neurospheres were then infected with HIV-1 dual tropic 89.6 (MOI:10) with
252 or without cART as described above. After fourteen days, supernatants were collected and neurospheres were
253 harvested for downstream assays. As shown in Fig. 2e, western blot revealed robust expression of p24 capsid
254 protein with undetectable expression of Pr55, thus suggesting an efficient cleavage of the viral polyprotein in the
255 induced neurospheres relative to the uninfected sample. We also observed increased expression of the intracellular
256 forms (e.g. 30, 40 kDa) of the accessory protein Nef [65] relative to the uninfected sample. Again, treatment of
257 HIV-1 neurospheres with cART decreased the expression of both p24 and Nef.

258 Cytokine-treated neurospheres were also assessed via western blot to evaluate the expression of different
259 microglia markers (e.g. IBA-1, CD11b, CD45). Data in Fig. 2e indicates that IBA-1 expression was relatively
260 consistent among each sample, whereas slightly varying levels of expression of CD11b and CD45 were observed
261 between samples. Additionally, the expression levels of apoptotic proteins were evaluated to assess whether
262 cytokine treatment or cART had any potential effects on apoptosis (Fig. 2e). Here, expression of the pro-apoptotic
263 protein BAD increased after HIV-1 infection and was reduced in the presence of cART. Importantly, BAD
264 expression was undetectable in the uninfected and cART-only samples. While low levels of uncleaved PARP-1
265 were observed in the untreated and cART samples, we observed increased expression of the 24 kDa cleaved
266 fragment in the HIV-1 sample.

267 RT-qPCR for HIV-1 TAR and *env* confirmed the expression of these RNAs in the HIV-1 cytokine-treated
268 samples. Of note, similar amounts of both TAR and *env* (~ 10^8 copies each) were detected, suggesting that
269 increased viral processivity was occurring in these cultures (Fig. 2f). Again, treatment with cART resulted in
270 significant reductions of both TAR and *env* RNA relative to the HIV-1 sample. Collectively, this data suggests that
271 treatment of neurospheres with IL-34, M-CSF, and TGFβ-1 effectively enhanced viral replication and processivity
272 and that this may be attributed to the induction of a pro-myeloid phenotype. This data also indicates that cytokine
273 treatment alone, as well as cART alone, did not promote apoptosis in neurospheres.

274 We next sought to assess the potential effects of HIV-1 (89.6) on the expression levels of multiple proteins
275 or enzymes associated with different CNS cell types. To this end, western blot was performed to evaluate the
276 relative expression microglia-like cells ($CD11b^+$, $CD163^+$), astrocytes ($GFAP^+$, glutamine synthetase$^+$),
277 dopaminergic neurons (TH^+, $FOXA2^+$), GABAergic neurons ($GAD65^+$, $GAD67^+$), glutamatergic neurons ($BNPI^+$)
278 and NSCs ($SOX2^+$). As shown in Fig. 3a, HIV-1 appeared to increase the expression of differentiated neurons,

279 particularly TH^+, $GAD65^+/GAD67^+$, and $BNPI^+$ neurons, whereas treatment with cART restored the expression of
280 these markers to levels that were comparable to the uninfected sample. A similar pattern of expression was also
281 observed for GFAP, while the expression of CD11b appeared relatively consistent between the uninfected, HIV-1
282 infected, and cART samples. On the other hand, expression of CD163 appeared to slightly decrease in both the
283 HIV-1 and cART samples relative to the uninfected sample.

284 As an additional control, we also evaluated the effects of co-culturing neurospheres with the HTLV-1
285 infected cell line HUT 102. HTLV-1 is the etiologic agent of HTLV-1-associated myelopathy/tropical spastic
286 paraparesis (HAM/TSP), a neurological disorder that is characterized by chronic neuroinflammation and
287 neurodegeneration [66, 67, 68, 69]. Prior to initiating the co-culture, HUT 102 cells were exposed to ionizing
288 radiation (IR) to inhibit chromosomal replication and to activate viral transcription, as previously described [70, 71,
289 72]. Treatment with a combination of IFN/AZT was also included to model the current standard for HTLV-1 anti-
290 viral therapy [73, 74, 75]. The irradiated HUT 102 cells served as the background control. After fourteen days of
291 co-culture, neurospheres were harvested for downstream assays. Data in Fig. 3a shows that HTLV-1 co-culture
292 resulted in a slight increase in the expression of FOXA2 and BNPI neurons and that treatment with IFN/AZT
293 reversed this increase. On the other hand, HTLV-1 appeared to reduce the expression of both CD11b and glutamine
294 synthetase relative to the uninfected sample, whereas IFN/AZT did not appear to have any impact. While the
295 expression of NSCs appeared relatively faint in the uninfected and HIV-1 samples, its expression was undetectable
296 in the HTLV-1 samples. These results are not entirely surprising as neurospheres were cultured in medium that was
297 enriched to induce differentiation into more mature cell types.

298 To confirm whether HTLV-1 was capable of replicating in neurospheres, western blot was performed to
299 assess the expression of HTLV-1 Tax and matrix (p19) proteins. As shown in Fig. 3b, the expression of both Tax
300 and p19 was higher after co-culturing of neurospheres with irradiated HUT 102 cells (relative to the background
301 control), thereby indicative of increased viral replication. As expected, treatment with IFN/AZT reduced the
302 expression of Tax and p19 to levels that were similar to the background control. Furthermore, RT-qPCR for HTLV-
303 1 *tax*, *env,* and *hbz* RNA showed that the expression of these RNAs significantly increased after co-culture and that
304 treatment with IFN/AZT resulted in a significant reduction of both *tax* and *env* transcripts (Fig. 3c).

305 Overall, these results demonstrate the ability of HIV-1 to replicate in NPC-derived neurospheres, therefore
306 indicating that these models may be permissive to infection. Moreover, our data suggests that the exposure of

307 neurospheres to microglia-inducing cytokines may enhance their susceptibility to infection. While the primary focus
308 of this manuscript remains on HIV-1, the data generated from the HTLV-1 experiments confirms the susceptibility
309 of neurospheres to retroviral infection and lays the foundation for future experiments focused on HTLV-1 or other
310 retroviral infections. Lastly, this data also points towards the differential effects of viral infection on the cellular
311 composition of neurospheres. Since neurospheres are composed of a heterogeneous population of cell types,
312 including those that are infected and uninfected, this area of research deserves further attention.

313 **The Effect of Stem Cell EVs on HIV-1 Infected Neurospheres**

314 Our experiments have shown receptor mediated alterations post-infection, indicating cellular damage.
315 Therefore, there is a need for a "holistic" reparative approach to potentially control cellular damage and regulate
316 inflammation. There is mounting evidence that EVs from different sources of stem cells, namely MSCs and iPSCs,
317 possess broad reparative and regenerative properties across various pathologies, including those related to the CNS
318 [43, 44, 45, 46, 47, 48]. Whether or not these vesicles confer reparative effects in the context of infection remains
319 relatively unexplored, especially with respect to the CNS. Our previous research pointed towards the potential
320 reparative effects of both MSC and iPSC EVs in 2D cultures of neurons, astrocytes, and monocyte-derived
321 macrophages (MDMs) damaged by IR [76]. Therefore, we sought to expand upon these studies by investigating the
322 potential functional effects of MSC and iPSC EVs in HIV-1 infected neurospheres.

323 The EVs used for these experiments were isolated using a scalable platform which incorporated the use of
324 tangential flow filtration (TFF) [76]. This advanced technology has the ability to produce large batches of highly
325 concentrated material in an efficient and reproducible manner and in recent years its application for EV isolation has
326 been well documented by others [77, 78, 79, 80]. Here, we include data from the analysis of MSC and iPSC EVs;
327 we also include data from A549 (cancer) EVs which served as both a control for our EV isolation method as well as
328 a non-stem cell control. NTA analysis shows that the size distribution of each EV preparation falls within the range
329 of 50 to 250 nm (Fig. 4a). Consistent with our previous research, iPSC EVs and A549 EVs appear more
330 heterogeneous in their size distribution relative to MSC EVs [76]. TEM of each EV preparation also confirmed the
331 presence of cup-shaped vesicles that appeared less than 200 nm in diameter. Representative TEM images from each
332 EV preparation are included in Fig. 4b. Interestingly, these images also showed that iPSC EVs tended to cluster
333 together in aggregates of smaller (~50 nm) vesicles whereas MSC EVs appeared as both larger (~100 nm) vesicles
334 and aggregates of smaller (~50 nm) vesicles.

335 To assess the efficiency of their uptake by differentiated neurospheres, EVs were fluorescently labeled with
336 a commercially available dye which stains both neutral and nonpolar lipids (BODIPY). Labeled EVs were then
337 added to cultures of differentiated neurospheres. As shown in Fig. 4c, fluorescent microscopy initially revealed a
338 relatively weak and diffuse signal that persisted throughout the first 48 hours (day 2). However; over time, the
339 fluorescent intensity increased. Representative photographs (day 8) show a strong fluorescent signal that appeared
340 to be predominantly localized in the center of each EV-treated neurosphere. We also observed similar results when
341 treating neurospheres with EVs labeled with the SYTO RNASelect nucleic acid stain (Supplementary Fig. 2a).
342 Additionally, image analysis of EV-treated, cross-sectioned neurospheres pointed towards a strong and relatively
343 even EV uptake, with fluorescent signal being detected in cells throughout the center and periphery of the spheres
344 (Supplementary Fig. 2b). Interestingly, we also observed a change in the diameter and morphology of EV-treated
345 neurospheres over time. Data in Fig. 4d shows representative images taken two weeks-post EV treatment. Here,
346 EV-treated neurospheres appeared larger in size and the borders were relatively less well-defined as compared to the
347 untreated neurospheres. Quantification of neurosphere diameter confirmed that EV-treated neurospheres were
348 significantly larger in size relative to untreated neurospheres (Fig. 4e and Supplementary Figure 2c).
349 Given our observation that EV-treated neurospheres displayed a change in morphology that was
350 characterized by a slight reduction in their well-defined spherical border, we next questioned whether EVs may
351 contain enzymes capable of degrading the extracellular matrix within neurospheres. To address this, we performed
352 western blot for matrix metalloproteinase 9 (MMP9), as it is one of the most well-studied members of the MMP
353 family and, interestingly, has also been associated with reparative and regenerative functions in the CNS [81, 82].
354 Results from this experiment revealed MMP9 expression in both iPSC and A549 EVs, while its expression was
355 undetected in MSC EVs (Supplementary Fig. 2d). As a follow-up, we performed gelatin zymography, as this is a
356 reliable assay to assess the relative proteolytic activity of experimental samples [83, 84]. Imaging of the stained gel
357 indicated the presence of active MMP9 as well as active MMP2 in each EV prep. Among the samples A549 EVs
358 displayed the highest intensity, followed by iPSC and MSC EVs (Supplementary Fig. 2e). This data suggests that
359 EVs are capable of not only penetrating, but also persisting in, three-dimensional cultures and, moreover, that EV-
360 associated proteolytic enzymes may partially contribute to this effect.
361 After confirming EV uptake by neurospheres we focused next to examine their potential functional effects
362 in HIV-1 infected neurospheres. To date, the anti-apoptotic effects of stem cell EVs in the context of the CNS have

363 been well documented both *in vitro* and *in vivo* [85, 86, 87, 88, 89, 90]. To this end, we performed western blot to
364 examine the expression levels of different pro-apoptotic proteins (Fig. 5a). Relative to the uninfected control
365 sample, HIV-1 was associated with a slight increase in the expression of cleaved PARP-1 as well as a moderate
366 increase in the expression of both Caspase 3 and BAD. Furthermore, the addition of cART was associated with an
367 increased expression of cleaved Caspase 3 and BAD relative to the HIV-1 sample. However, the addition of cART
368 in combination with EVs (iPSC, MSC EVs, and A549) decreased the expression of cleaved PARP-1 (24 kDa),
369 Caspase 3 (cleaved and uncleaved), and BAD relative to HIV-1 + cART. As an additional control, we included
370 treatment of uninfected neurospheres with cART (lane 3). The expression of each protein in this sample was
371 relatively consistent with those of the uninfected control, suggesting that cART alone did not have a toxic effect on
372 the neurospheres.

373 In addition to their anti-apoptotic effects, stem cell EVs are also associated with potent anti-inflammatory
374 properties and several recent studies have highlighted their ability to reduce neuroinflammation in various models of
375 CNS damage [91, 92, 93, 94, 95, 96]. To assess the potential anti-inflammatory effects of stem cell EVs on HIV-1
376 infected neurospheres, we performed western blot for well-known pro-inflammatory mediators (Fig. 5b). Here,
377 substantial increases in TNFα, IL-8, and IL-1β were observed after HIV-1 infection. Treatment with cART
378 decreased expression of soluble IL-1β to an undetectable level while only slightly decreasing the expression of
379 TNFα and IL-8. Notably, similar results were also observed in JR-CSF and CHO40-infected neurospheres
380 (Supplementary Fig. 3). Again, in HIV-1 89.6-infected neurospheres, the combination of cART with either iPSC or
381 MSC EVs restored the expression of TNFα, IL-8 and IL-1β to levels that were comparable to the uninfected control.
382 Interestingly, similar results were observed with A549 EVs. Taken together, this data indicates that EVs are capable
383 of exerting both neuroprotective and anti-inflammatory effects in HIV-1 infected neurospheres. Overall, these
384 findings are in consensus with the pre-existing literature on stem cell-derived EVs. Given that A549 EVs originate
385 from cancer cells, a more thorough assessment of the functional effects associated with cancer EVs is required to
386 evaluate the long-term consequences in recipient cells.

387 **RNA Analysis of Stem Cell EVs**

388 The reparative aspects of stem cell EVs have been shown to be associated with various non-coding RNAs
389 and/or proteins that confer protective and/or immunomodulatory functions in damaged recipient cells [97, 98, 99,
390 100, 101]. While several recent studies have extensively characterized the miRNA profiles of stem cell EVs, the

391 characterization of EV-associated long non-coding RNAs (lncRNAs) remains a relatively unexplored topic [41, 102,
392 103, 104]. Our previous studies included the sequencing of lncRNAs (≥ 250 base pairs) from iPSC, MSC, and A549
393 EVs [76]. Again, the purpose of including A549 EVs was to serve as a non-stem cell control. Here, we share an
394 expanded set of data from our initial studies to highlight the differences that exist among these different EV
395 populations.

396 Overall, approximately 6.5 x10^7, 1.9 x 10^7, and 2.6 x 10^7 valid reads were obtained from iPSC, MSC, and
397 A549 EVs, respectively, with each preparation having a Q30 score greater than 85% (Supplementary Table 1). Of
398 these reads, approximately 80.88% (iPSC EVs), 71.21% (MSC EVs), and 70.66 (A549 EVs) were mapped to the
399 genome. As shown in Fig. 6a, the majority of lncRNAs among each EV preparation mapped to introns. iPSC EVs
400 had the highest number of intronic transcripts (93%) followed by MSC EVs (79%) and A549 EVs (75%). The
401 percentage of transcripts mapping to either exons or intergenic regions ranged from approximately 10 to 15% among
402 MSC and A549 EVs; however only ~3% of transcripts from iPSC EVs were mapped to these regions.

403 Transcripts that were not annotated in genome annotation databases were subsequently designated as novel
404 transcripts according to the following class codes: i = transfrag falling within a reference intron; j = potentially novel
405 isoform with at least one splice junction shared with a reference transcript; o = generic exonic overlap with a
406 reference transcript; u = unknown intergenic transcript; x = exonic overlap with reference on the opposite strand.
407 Data in Fig. 6b shows that within each EV prep, the majority of transcripts either fell within a reference intron (i)
408 (> 50%) or were classified as unknown intergenic transcripts (u) (< 40%) and, moreover, that ≤ 0.1% of transcripts
409 among each sample were classified as either "j", "o", or "x".

410 Volcano plots in Fig. 6c provide a visual representation of the differentially expressed transcripts between
411 iPSC and A549 EVs (Fig. 6c, left panel) and between MSC and A549 EVs (Fig. 6c, right panel). Transcripts
412 displaying statistically significant regulation (either up or down) are annotated with their associated gene
413 ID/transcript name. Overall, these plots reveal that a majority of transcripts associated with stem cell EVs are
414 downregulated relative to A549 EVs. Additionally, iPSC EVs displayed a greater amount of significantly up-
415 regulated transcripts relative to MSC EVs when compared to A549 EVs. Notably, transcript MSTRG.106597 was
416 among the most significantly upregulated transcript associated with both iPSC EVs and MSC EVs and its
417 approximate fold change relative to A549 EVs was 3392 for iPSC EVs and 229 for MSC EVs. For reference, this is
418 designated as a novel transcript which corresponds to gene FP671120.1. Heat maps generated from all EV-

419 associated lncRNA transcripts are included in Supplementary Fig. 4a and show the comparisons between iPSC and
420 A549 EVs (left panel) and between MSC and A549 EVs (right panel). Annotated transcripts were further analyzed
421 by performing Gene ontology (GO) (Supplementary Fig. 4b-c). Relative to A549 EVs, iPSC EVs had significantly
422 enriched GO terms which included RNA and protein binding, positive regulation of GTPase activity and cell
423 adhesion. Relative to A549 EVs, MSC EVs had significantly enriched GO terms which included RNA binding,
424 protein binding, and T cell receptor signaling pathway. Chromosome maps of EV-associated lncRNA transcripts
425 revealed striking differences in the density distribution when comparing stem cell EVs and A549 EVs. Specifically,
426 transcripts from A549 EVs appeared more evenly distributed and spanned all chromosomes while transcripts from
427 iPSC and MSC EVs only mapped to certain chromosomal regions (Supplementary Fig. 4d).
428 The heatmap comparing the expression of all lncRNA transcripts between iPSC and MSC EVs is shown in
429 Supplementary Fig. 5a and the corresponding volcano plot is show in Supplementary Fig. 5b. Of note, this graph
430 shows a relatively even distribution of up- and down-regulated transcripts. Collectively, this data reveals distinct
431 differences in the expression of lncRNA transcripts associated with EVs derived from stem cells versus cancer
432 (A549) cells. Future studies will include a more thorough assessment of the differentially expressed transcripts
433 among iPSC and MSC EVs and will focus on their potential functional implications.

434 **Detection of RNA Binding Proteins Using RNA Pull-down Assay**

435 In an effort to define the role of EV-associated lncRNAs and to better understand their potential functional
436 significance in recipient cells, we recently identified at least one lncRNA transcript associated with iPSC EVs
437 (AC120498.9) which possessed a unique secondary structure [76]. Specifically, this transcript contained two
438 continuous stretches of double-stranded RNA that were greater than 30 base pairs (bp) in length, a property that has
439 previously been associated with the activation of PKR [105, 106]. This prompted us to further examine the
440 secondary structures of other EV-associated lncRNAs, first by focusing on those that were more highly associated
441 with iPSC EVs. We subsequently generated secondary structures from over 240 iPSC EV-associated lncRNAs that
442 had FPKM values of ≥ 2 relative to MSC and A549 EVs. From this analysis we identified another transcript
443 (ADIRF-AS1) which also contained a continuous stretch of double-stranded RNA greater than 30 bp. For reference,
444 the secondary structures of ADIRF-AS1 and AC120498.9 are shown in Fig. 7a. RT-qPCR confirmed that both of
445 the relevant sequences shown in Fig. 7a (i.e. double-stranded RNA greater than 30 base pairs) were detected in EVs
446 and that their expression was significantly increased in iPSC EVs relative to MSC EVs (Fig. 7b).

447 To assess whether the identified sequences were capable of binding to PKR the biotin-conjugated synthetic
448 RNA sequences were incubated with whole cell lysate from the neuronal cell line SHSY5Y and then purified using
449 Streptavidin-Sepharose beads. Western blot was performed to assess the expression of PKR, as well as other critical
450 RNA binding proteins. The results in Fig. 7c confirm that the relevant sequences from both ADIRF-AS1 and
451 AC120498.9 were capable of binding not only to PKR, but also to other double stranded RNA (dsRNA) binding
452 proteins including DICER and ADAR1. We additionally performed similar experiments using whole cell lysate
453 from either astrocytes or MDMs (Supplementary Fig. 6). Again, western blot analysis confirmed expression of
454 PKR, DICER, and RIG-I, thereby highlighting the potential of these RNAs to bind to multiple different RNA
455 binding proteins in CNS relevant cell types. As a negative control for these experiments, we did not detect
456 expression of p65 (data not shown). Collectively, we suspect that these innate immune molecules may bind to EV-
457 associated lncRNAs to either activate their enzymatic activities or, alternatively, to suppress their functions in
458 recipient cells. Future studies will better focus on the potential significance of this binding.

459 **Stem Cell EVs Rescue Cellular Viability in HIV-1 Damaged Neurons**

460 Based on the above data showing that NPC-derived neurospheres are susceptible to HIV-1 infection and
461 that stem cell EVs may exert neuroprotective effects, we next assessed the potential functional effects of stem cell
462 EVs on damaged neurons *in vitro*. Here, we utilized two-dimensional cultures of the neuronal cell line SHSY5Y; to
463 induce neuronal damage cells were exposed to EVs derived from U1 (HIV-1 infected) cART-treated cells
464 ("damaging EVs"). Our rationale was based on results from previous studies showing that EVs from HIV-1 infected
465 cells contain viral by-products (e.g. TAR, Tat, Nef, *env*) that can be transferred to recipient cells [107, 108, 109,
466 110]. Thus, we hypothesized that exposure of neurons to these damaging EVs would be characterized by a loss in
467 cellular viability and, moreover, that stem cell EVs may have the potential to reverse this effect.

468 For this assay SHSY5Y cells were treated with EVs from either U1 cART-treated cells or a combination of
469 U1 cART EVs with stem cell EVs. Representative images in Fig. 7d show that after approximately eight days in
470 culture the untreated cells appeared healthy, well-attached, and exhibited a spindle-like morphology. Conversely,
471 neurons exposed to U1 cART EVs displayed an altered appearance that was characterized by a reduction in
472 attachment and clumping/ aggregation of the remaining attached cells. However, treatment with either iPSC or
473 MSC EVs at an approximate ratio of 1:1000 (recipient cell: EV) promoted the re-attachment and spreading of cells
474 that more closely resembled the untreated control culture. To ascertain whether these effects may be mediated by

475 EV-associated RNA, stem cell EVs were exposed to UV(C) irradiation to deactivate RNA. Treatment of neurons
476 with irradiated EVs appeared to abrogate the morphological effects associated with non-irradiated stem cell EVs.
477 Cellular viability was next assessed using a luminescence-based assay. As shown in Fig. 7e, treatment of neurons
478 with U1 cART EVs resulted in a slight decrease in viability relative to the control. While the treatment with stem
479 cell EVs did improve cellular viability, only iPSC EVs were associated with a significant increase. Furthermore,
480 there were no significant effects of UV(C) irradiated EVs on cellular viability.
481 In a separate experiment, we have also utilized EVs isolated from cells infected with the human
482 coronavirus OC43 to induce neuronal damage (Supplementary Fig. 7). Similar to what was observed with U1 cART
483 EVs, neurons exposed to OC43 EVs detached from the substrate and appeared round in morphology. Again,
484 treatment with both iPSC and MSC EVs appeared to permit the re-attachment and spreading of cells. Exposure to
485 OC43 EVs also resulted in a strong reduction of neuronal viability and treatment with both iPSC and MSC EVs
486 significantly abrogated this effect. Moreover, exposure of stem cell EVs to UV(C) irradiation substantially inhibited
487 their ability to restore cellular viability. Collectively, these results suggest that stem cell EVs may at least partially
488 reverse the damaged phenotypes associated with infection. Future studies will focus on optimizing these
489 experiments to better characterize the mechanism(s) associated with virally induced damage and stem cell EV-
490 mediated repair.
491
492
493
494
495
496
497
498

499 **Discussion**

500 Throughout the last decade, iPSCs and their derivatives have revolutionized the fields of regenerative
501 medicine, drug development, and disease modeling [11]. With respect to the CNS, iPSC-derived NPCs and NSCs
502 have been used to successfully generate 3D neuronal cultures, or neurospheres. Relative to traditional 2D cultures,
503 3D models are expected to serve as a more relevant platform for the study of biological processes. For example,
504 neurospheres have the potential to provide enhanced molecular insight into key cellular processes relating to
505 migration, replication, apoptosis [27]. Additionally, their ability to be cultured in serum-free and chemically defined
506 conditions renders them particularly important for studies pertaining to neural development and neurogenesis [32].
507 Thereby, neurospheres may represent an ideal platform for preliminary *in vitro* studies surrounding the pathogenesis
508 of various neurological diseases and disorders. Previous works by others have utilized 3D neuronal cultures to
509 successfully model Zika and HSV-1 infections [33, 34, 35, 49]. More recently, Dos Reis et al. reported results
510 demonstrating that HIV-1 infected microglia could be incorporated into human brain organoids [36]. With respect
511 to HIV-1 infection, it is also important to note that a recent study by Rai et al. demonstrated that iPSC-derived
512 microglia displayed significant expression of both CD4 and CCR5 receptors and were readily infected by HIV-1
513 [111]. Importantly, we also have data demonstrating that our NPC-derived neurospheres, which were generated
514 from human iPSCs, express both CD4 and CCR5. Moreover, this expression remained relatively consistent after
515 treatment of infected samples with cART and EVs; this data further supports our claims regarding the susceptibility
516 of neurospheres to HIV-1 infection (Supplementary Fig. 8). To the best of our knowledge, this is the first study
517 utilizing human NPC-derived neurospheres for retroviral infection.

518 The use of well-characterized and qualified material, as well as the establishment of robust and
519 reproducible protocols is essential for ensuring the integrity of scientific data. The protocols employed here
520 permitted the efficient formation of neurospheres, resulting in well-defined cultures that displayed uniformity in size
521 and appearance throughout the duration of the study; thereby overcoming some of the challenges that have
522 historically been associated with use of 3D neuronal cultures [52]. The NPCs used for these experiments also
523 underwent extensive characterization to authenticate not only their identity, but also their differentiation potential.
524 Our data suggests that NPC-derived neurospheres maintain their ability to differentiate into both mature neurons
525 (e.g. dopaminergic, GABAergic, glutamatergic) and glial cells (i.e. astrocytes and potentially microglia) in 3D
526 cultures. It is worth noting that properly distinguishing between microglia and macrophages has historically been

527 challenging as these cell types are often associated with many of the same surface markers. Due to the difficulties
528 associated with their phenotypic identification, here we use the term "microglia-like cells" to correlate with positive
529 expression of either CD163, CD11b, CD45, and IBA-1 as these markers are associated with either resting or
530 activated microglia and macrophages [112, 113, 114, 115, 116]. While the potential of neurospheres to differentiate
531 into microglia remains a topic of debate, it is important to consider that the expression of cell-specific markers may
532 greatly vary in response to different biological and biochemical parameters such as cell maturation, cell culture
533 conditions, and the inherent phenotypic heterogeneity within a given cell type [117]. Along these lines, D'Aiuto et
534 al. recently utilized human iPSC-derived NPCs to generate scaffold-free adherent 3D neuronal cultures which
535 expressed not only neuronal (glutamatergic, GABAergic, dopaminergic) markers but also GFAP and IBA-1 [35]. In
536 addition, we suspect that exposure of neurospheres to a stimulating agent (e.g. LPS) could further promote the
537 expression of a microglial-like phenotype.

538 Despite being regarded as "immune privileged," the CNS contains at least three types of immune cells,
539 namely CD4+ T cells, macrophages, and microglia, that can be infected by HIV-1 and subsequently serve as viral
540 reservoirs [59]. In the CNS, HIV-1 can activate numerous inflammatory mediators and enzymes that disrupt
541 downstream signaling pathways in both neuronal and glial cells [118]. HIV-1 infection is also associated with a
542 range of neurological symptoms collectively known as HAND, and the release of toxic viral proteins by infected
543 cells is expected to contribute to HAND pathogenesis [5,6,7,8]. However, the underlying mechanisms remain
544 poorly understood; consequently, there is a need to develop advanced assays to better characterize the molecular
545 mechanisms that contribute to HAND and other HIV-1 associated disease phenotypes. In these studies we sought to
546 assess the feasibility of using NPC-derived neurospheres for future studies modeling HIV-1 infection.

547 Dual-tropic HIV-1 89.6 utilizes the CXCR4 and CCR5 coreceptors; both of which are expressed on
548 resident CNS cells including macrophages, microglia, and astrocytes [118]. Whether or not astrocytes can harbor
549 productive infection remains a matter of debate; although integrated HIV-1 has been detected in astrocytes isolated
550 from infected patients and it has been reported that infected astrocytes can produce viral proteins (e.g. Tat, Rev, Nef)
551 that contribute to neuroinflammation and neuronal damage [2, 59, 62, 119, 120, 121, 122]. Results from our
552 experiments confirmed viral replication in neurospheres as evidenced by the expression of p24 capsid protein,
553 uncleaved Gag polyprotein Pr55, and accessory protein Nef, all of which were detected after fourteen days in
554 culture. As a measure of validation, we also detected p24 in neurospheres exposed to two other lab-adapted strains

555 (JR-CSF and CHO40). IP assays further revealed that the highest copies of HIV-1 TAR DNA were associated with
556 microglia-like cells. The JR-CSF infected sample also displayed relatively high copy numbers of TAR DNA
557 associated with astrocytes; a finding that is not entirely surprising given that this viral isolate originated from the
558 cerebrospinal fluid of an infected patient.

559 Perhaps more importantly, our data suggests that treatment with IL-34, M-CSF, and TGFβ-1 for a period of
560 one week had the potential to induce a microglia-like phenotype in neurospheres. Notably, we also found that
561 cytokine-treated neurospheres harbored more efficient viral replication. To highlight this point, we observed
562 undetectable expression of Pr55 Gag polyprotein that corresponded with a robust expression of cleaved p24 capsid
563 protein. Moreover, the copy numbers of TAR and *env* RNA were relatively similar in cytokine-treated samples,
564 thus indicating an increased level of HIV-1 transcription in these cultures. When considering the mixed cellular
565 composition of differentiated neurospheres, which clearly retained a distinct proportion of NPCs (Fig 1.d), we
566 speculate that addition of IL-34, M-CSF, and TGFβ-1 induced these progenitor cells to differentiate in a
567 myeloid/microglia phenotype that was more permissible to HIV-1 infection.

568 Overall, this data is in agreement with HIV-1 tropism towards glial-like cells. However, whether HIV-1
569 DNA represents a mixture of both non-integrated DNA as well as integrated proviral DNA in neurospheres has not
570 been quantitatively analyzed. Along these lines we have recently performed preliminary integration experiments
571 (Supplementary Fig. 9) adapted from previously published *Alu* PCR protocols [123, 124, 125, 126]. While the data
572 generated from these experiments suggests a mixture of both integrated (> 50%) and unintegrated (< 50%) HIV-1
573 DNA, it does not specifically address factors relating to site of integration and does not distinguish between cell
574 types infected (i.e. astrocytes vs. microglia). For example, in the cART samples, although integrated copies (Alu-
575 *gag*) are increased (i.e. lower Ct value) relative to unintegrated copies (*Gag*-only), this does not address whether the
576 integrated copies are from astrocytes or microglia or whether unintegrated DNA are preferentially increased in one
577 cell type over another. Therefore, our future experiments will have to carefully address a number of issues including
578 the location of integration in each cell type prior to cART and post-cART, and whether there is a difference in
579 integration depending on the viral strain used (e.g. dual tropic vs. neurotropic). These complex sets of questions
580 can, however, be addressed in "3D" neurosphere models, especially if we are able to maintain long-term cultures
581 over a period of three to six months prior to genome analysis.

582 Interestingly, we observed unique expression profiles of cell-specific markers among uninfected and

583 infected neurospheres (Fig. 3a). First, these results are in general agreement with our previous assays (ICC and IP)
584 which relied on the use of antibodies associated with astrocytes (GFAP), microglia-like cells (CD11b, CD163),
585 neurons (FOXA2, GAD65), and NSCs (SOX2) as varying levels of expression for each of these markers was
586 detected. GFAP is an intermediate filament protein that is most commonly associated with astrocytes and increased
587 GFAP expression is a hallmark of astrocyte activation (e.g. astrogliosis or astrocytosis) [127, 128]. Our observation
588 of increased GFAP expression in HIV-1 infected neurospheres is consistent with previous literature that has
589 characterized HIV-1 infection by astrocytosis [129, 130, 131]. As indicated previously, CD11b is an integrin
590 protein that can be used to identify either resting or activated microglia-like cells. Our observation of relatively
591 consistent CD11b expression may be related to the specificity of the antibody used. While the apparent increase in
592 the expression levels of neuronal markers (TH^+, $GAD65^+/67^+$, $BNPI^+$) in HIV-1 infected neurospheres were
593 unexpected, further studies are warranted to see if this phenotype reproduces. Without having an accurate
594 quantification of the cellular composition of neurospheres, it cannot be ruled out that some samples had inherently
595 higher levels of certain cell types to begin with. In addition, the spatial location of certain cell types within each
596 sphere needs to be considered. Without knowing the kinetics of HIV-1 infection in this 3D platform, it is also
597 possible that the virus was not able to efficiently penetrate the neurospheres; along these lines, an incubation period
598 longer than fourteen days may be required to better assess the long-term effects of HIV-1 infection on certain cell
599 types. Nonetheless, we believe that these novel results provide a justifiable proof-of-concept for continued studies
600 that can further fine tune these experimental details.
601 The primary focus of this manuscript surrounds retroviral infections, namely HIV-1 and HTLV-1. HTLV-
602 1 is the etiological agent of both adult T cell leukemia (ATL) and the progressive neurological disorder known as
603 HTLV-1-associated myelopathy/tropical spastic paraparesis (HAM/TSP) [66, 67, 68, 69]. As in the case of HIV-1,
604 the underlying mechanisms contributing to HTLV-1 associated pathologies remain poorly understood. Thus, there
605 is an imminent need for the identification of suitable *in vitro* platforms to drive the field of HTLV-1 research.
606 Exposure to IR is known to initiate cell cycle arrest; moreover, we have recently published data using IR to activate
607 transcription of HTLV-1 in HUT 102 cells [70, 71, 72, 132]. Therefore, we rationalized that co-culturing of
608 irradiated HUT 102 cells with neurospheres would provide a reliable platform to assay for infection. To this end, we
609 performed western blot to assess the relative expression of Tax and p19, two indicators of HTLV-1 viral replication.
610 When accounting for background levels in the non-irradiated HUT 102 control sample, there were clear increases in

611 the expression of both Tax and p19. RT-qPCR also confirmed increased expression of *tax, env*, and *hbz* in the co-
612 cultures. Treatment with IFN/AZT was also associated with reductions in the corresponding protein/gene
613 expression levels. Therefore, this preliminary data suggests that neurospheres may be reliable models for studying
614 the mechanisms surrounding HTLV-1 associated neuropathogenesis. Future experiments will utilize other HTLV-1
615 and HIV-1 infected cells (e.g. U1 cells) that have been irradiated to potentially increase viral spread.

616 In recent years our laboratory has also focused extensively on EVs and considerable efforts have been
617 made in the characterization of EVs from both infected and non-infected cells [72, 76, 108, 109, 110, 133, 134, 135].
618 Here specifically, we were interested in examining the functional effects of stem cell EVs on HIV-1 infected
619 neurospheres. Our rationale was based on the results from numerous studies which have highlighted the protective
620 and reparative properties of stem cell EVs among various CNS pathologies, as reviewed elsewhere [43, 48, 48, 136].
621 For these studies we utilized well-characterized preparations of iPSC and MSC EVs that have previously
622 demonstrated reparative effects in various *in vitro* assays (e.g. cellular migration, cellular viability, angiogenesis)
623 [76].

624 The results from our uptake assays first confirmed that EVs were capable of penetrating neurospheres.
625 Moreover, fluorescently labeled EVs remained detectable for at least eight days post-treatment. These results were
626 consistent among two independent experiments that used different fluorescent probes to stain either EV lipid
627 membranes or EV-associated RNA. Interestingly, gelatin zymography indicated that iPSC and A549 EVs had
628 relatively high levels of the active forms of the gelatinases MMP9 and MMP2 as compared to MSC EVs. While we
629 observed distinct differences in the morphological appearance of iPSC EV and A549 EV-treated neurospheres, it is
630 imprudent to attribute this effect to any specific EV cargo at this time. More importantly, these results demonstrated
631 feasibility and provided the justification for subsequent experiments focused on the functional effects of stem cell
632 EVs in neurosphere cultures.

633 As previously mentioned, over amplification of inflammatory pathways, coupled with the release of toxic
634 viral proteins from infected cells, is believed to contribute to the neuronal damage associated with HIV-1 [5,6,7,8].
635 Additionally, activated microglia release neurotoxic factors including cytokines and chemokines (e.g. IL6, IL8,
636 IL1β, TNFα, IFNα) that can further exacerbate the inflammatory response [61, 118]. In recent years, the
637 neuroprotective and anti-inflammatory properties of stem cell EVs have been well-documented; in the context of the
638 CNS, there is accumulating evidence that stem cell EVs may be able to reverse neuronal apoptosis and modulate the

639 polarization of both astrocytes and microglia from pro-inflammatory to anti-inflammatory phenotypes [85, 86, 87,
640 88, 89, 90, 91, 92, 93, 94, 95, 96]. To the best of our knowledge, the functional effects of stem cell EVs on 3D
641 cultures has not previously been reported.

642 As expected, we observed increased expression of pro-inflammatory cytokines TNFα, IL-8, and IL-1β in
643 HIV-1 infected neurospheres. Additionally, we also observed increased expression of both cleaved PARP-1,
644 Caspase-3, and BAD in response to HIV-1 infection. These findings are consistent with the activation of cellular
645 stress response pathways and the initiation of apoptotic signaling cascades [137, 138, 139]. The addition of stem
646 cell EVs to HIV-1, cART-treated neurospheres abrogated each of these effects; thereby pointing towards a potential
647 EV-mediated reversal of inflammatory and apoptotic signaling in these cultures. Since Caspase 3 is classically
648 regarded as an "executioner" caspase [140, 141] this data also suggests that damaged cells may have been in the
649 early stages of apoptosis, thus making them more receptive to reparative intervention by EVs. While our data
650 suggests that A549 (cancer) EVs may also exert anti-apoptotic and anti-inflammatory properties, further
651 interpretation and analysis of these results is outside the scope of the current manuscript. Unlike stem cell EVs, the
652 use of cancer EVs for potential repair is not well-studied and the long-term functional outcomes associated with
653 exposure to cancer EVs needs to be better characterized.

654 Although the results from these experiments aren't cell-type specific, our future experiments will more
655 thoroughly examine which cell types in neurospheres are associated with increased levels of apoptosis.
656 Additionally, our future experiments will focus on examining the expression levels of other critical mediators of
657 apoptosis, including p53 and its kinases (e.g. ATM, ATR), as well as a broader range of proteins involved in the
658 early, middle, and late stages of apoptosis to better define the reparative mechanisms of stem cell EVs.

659 EVs are associated with a rich diversity of cargo which includes various non-coding RNAs (i.e. small non-
660 coding and long non-coding RNAs), as described elsewhere [142, 143, 144, 145, 146, 147]. Mechanistically
661 speaking, this cargo is expected to drive the functional effects that are attributed to EVs. While many studies have
662 evaluated the reparative potential of various EV-associated miRNAs, the characterization of EV-associated
663 lncRNAs remains largely unexplored. The data from our lncRNA analysis highlighted distinct differences among
664 A549 (cancer) EVs and stem cell EVs, particularly with respect to chromosome localization and patterns of
665 differentially expressed transcripts. Although lncRNAs from both iPSC and MSC EVs mapped to some
666 chromosomes as compared to A549 EVs, it is difficult to decipher the functional significance of this data in the

667 absence of mutant reagents. For instance, iPSC and MSC EVs contain lncRNAs that map to certain chromosomes;
668 however, it is not clear if the same EVs that contain these RNAs also contain cytokines and reparative proteins.
669 Furthermore, the actual copy number of these RNAs in various subpopulations of EVs (e.g. those ranging from ~30
670 to 220 nm in size) requires further purification, followed by functional repair assays and then proteomics and RNA
671 seq. This will better define which EV subtype contains cytokines, proteins, and RNAs that map to a certain
672 chromosome. Therefore, future experiments will better define the type of EVs needed to repair, as well as their
673 protein and RNA cargo that may functionally regulate either the host genome, splicing in the nucleus, translation
674 inhibition, or mRNA degradation in the cytoplasm.

675 The identification of at least two iPSC EV-associated lncRNAs (i.e. AC120498.9, ADIRF-AS1) whose
676 secondary structures contained sequences of double-stranded RNA ≥ 30 bp in length led us to examine their
677 interactions with different RNA binding proteins *in vitro*, as this property has previously been linked to the
678 activation of PKR [105, 106]. In an attempt to decipher their function, our data indicates that these EV-associated
679 lncRNAs may regulate PKR, RIG-I, Dicer, and potentially eIF2α phosphorylation. However, it is not clear at this
680 point whether the binding of innate immune molecules to these RNAs results in their increased stability or change of
681 enzymatic function. Additionally, when mapping the secondary structures of iPSC EV-associated lncRNAs, we
682 noted that many of these each contained multiple circular loops that resemble the structure of circular RNAs
683 (circRNAs). For reference, we have included a panel of images of these structures in Supplementary Fig. 10. While
684 circRNAs represent a relatively novel class of non-coding RNAs, there is emerging evidence to suggest that they
685 may predominantly function as miRNA sponges to prevent binding of miRNAs to their target genes [148, 149].
686 Therefore, we speculate that these structures could potentially serve as RNA sponges for cellular miRNA that
687 regulate pathways such as apoptosis, cell cycle, and cytokine secretion. Future experiments will better define how
688 these stem and loop RNA structures are capable of binding to dsRNA proteins and how they may also regulate
689 miRNAs that may be essential for cellular repair in damaged cells.

690 It has been shown that EVs released from HIV-1 infected cells contain viral by products including Nef, Tat
691 *env*, and TAR [107, 108, 110, 150]. The effects of these damaging EVs include rendering recipient cells more
692 susceptible to infection, enhancing the spread of infection, and induction of cellular death, as recently reviewed
693 [151]. Since we were unable to directly study their effects in HIV-1 infected neurospheres, we utilized 2D cultures
694 of neurons to determine if exposure to EVs from HIV-1 infected cells could induce neuronal death and,

695 subsequently, to assess whether stem cell EVs could exert any functional effects on damaged cells. Our data
696 confirmed a decline in cell healthy and slight reduction in viability upon treatment with damaging EVs, while stem
697 cell EVs appeared to reverse these processes. Even though UV(C) treatment did not have a significant impact on
698 cellular viability, the observed morphological differences in neurons treated with irradiated stem cell EVs relative to
699 non-irradiated EVs suggests that UV(C) may have partially impaired the functional effects of both iPSC and MSC
700 EVs. On the other hand, performance of the same assay using OC43 EVs to induce neuronal damage produced
701 considerable outcomes. Here, treatment of damaged cells with stem cell EVs yielded a significant increase in
702 viability whereas UV(C) irradiation abrogated their effects. Thus, these experiments highlight the existence of
703 different mechanisms surrounding both EV-induced damage and EV-mediated repair in recipient cells.
704 Overall, the results from this study have demonstrated that NPC-derived neurospheres are susceptible to
705 retroviral infection and, therefore, may serve as an alternative platform for studying the molecular mechanisms
706 associated with HIV-1. Moreover, we also demonstrated the functional relevance of stem cell EVs in the context of
707 mediating cellular repair induced by viral damage. Importantly, this data is in consensus with numerous other
708 studies which have described the neuroprotective and anti-inflammatory properties of stem cell EVs. We
709 acknowledge that further experiments are necessary to more carefully define and characterize the mechanisms
710 contributing to both viral-induced damage and EV-mediated repair. However, based upon the current data, we
711 hypothesize that the functional effects of stem cell EVs in both uninfected and virally infected cells may be partially
712 mediated through the interactions between EV-associated lncRNAs and nucleic acid sensors (e.g. PKR, ADAR1,
713 RIG-I) in recipient cells. For example, in uninfected cells this binding could trigger the activation of intracellular
714 signal transduction pathways, thereby resulting in increased production of interferon and a potent antiviral response
715 that may ultimately protect the cell from viral infection. Conversely, infected cells would have already mounted an
716 immune response to undergo cell cycle arrest. In this scenario, EV-associated lncRNAs could prolong this effect by
717 binding to, and thus inactivating, the host innate immune molecules to prevent further viral replication. In turn, this
718 would also dampen the production of damaging EVs from infected cells. Over time, the EV-associated cytokines
719 and growth factors will promote cellular replication of both infected and uninfected cells. However, we believe that
720 the net outcome will confer an overall protective effect, since we suspect that uninfected cells represent a majority
721 (≥ 90%) of the total cell population. In support of this, we have data showing that treatment of HIV-1 infected
722 neurospheres with stem cell EVs results in increased expression of different cell populations including NPCs,

723 astrocytes, and microglia-like cells (data not shown). Thus, we believe that this research sets an important precedent
724 for the continued use of NPC-derived neurospheres for modeling biological processes relating to the CNS. We look
725 forward to utilizing these cultures to further expand our knowledge in this area.

726
727
728
729
730
731
732
733
734
735
736
737
738
739
740
741
742
743
744
745
746
747
748
749
750
751
752
753

754 **Methods**

755 **Cell Culture**

756 **NPCs and Neurospheres**

757 Normal Human Neural Progenitor Cells (ATCC ACS-5003) were expanded per the manufacturer's
758 recommendations. Cells were cultured with STEMdiff Neural Progenitor Medium (STEMCELL technologies) in
759 cell matrix-coated flasks. Media was changed every other day. Cells were subcultured using Accutase diluted 1:1
760 with PBS. To generate neurospheres, NPCs were seeded at approximately 1.0 x 10^5 cells per well in ultra-low
761 attachment, U-shaped bottom 96-well plates in Neural Progenitor Medium. After approximately 48 to 72 hours, the
762 medium was removed from the wells and replaced with DMEM:F12 (ATCC 30-2006) + Dopaminergic Neuron
763 Differentiation Kit (ATCC ACS-3004) to induce differentiation. Neurospheres received a complete media
764 replacement every two to three days for a period of two weeks. Phase contrast images were acquired using an
765 inverted microscope and calibrated measurements were performed using Zen imaging software (Zeiss).

766 To further induce differentiation in neurospheres, the fully supplemented differentiation medium (listed
767 above) was spike with the following cytokines: IL-34 (100 ng/mL), M-CSF (25 ng/mL), and TGFβ-1 (50 ng/mL).
768 Neurospheres were cultured in this medium for an additional seven days, receiving fresh treatments every two to
769 three days, prior to HIV-1 infection.

770 **Cell Lines**

771 The human neuroblastoma cell line SHSY5Y (CRL-2266), the human astrocytoma cell line CCF-STTG1
772 (CRL-1718), human monocytic leukemia cell line THP-1 (TIB-202), and the human lung carcinoma cell line A549
773 (CCL-185) were obtained from the American Type Culture Collection (ATCC). SHSY5Y cells were cultured in a
774 1:1 mixture of EMEM (ATCC 30–2003) and F-12K (ATCC 30–2004) supplemented with 10% fetal bovine serum
775 (FBS) (ATCC 30–2020). CCF-STTG1 and THP-1 cells were cultured in RPMI-1640 (ATCC 30–2001)
776 supplemented with 10% FBS. A549 cells were cultured in F-12K (ATCC 30–2004) supplemented with 10% FBS.
777 Cells were maintained in culture following the manufacturer's recommendations. HIV-1 infected U937 Cells (U1;
778 NIH AIDS Reagent Program) were cultured in RPMI-1640 supplemented with 10% exosome-depleted FBS.

779 To generate MDMs, THP-1 cells and U1 cells were treated with phorbol 12-myristate 13-acetate (PMA;
780 100 nM) and incubated for four to five days. U1-MDMs then received two treatments of cART (emtricitabine,
781 tenofovir disoproxil fumarate, ritonavir, darunavir; 2.5 μM each) over a five day incubation period.

782 **Immunocytochemistry (ICC)**

783 Cells were fixed in 4% paraformaldehyde. Neurospheres were embedded in OCT and sectioned at a
784 thickness of 8 µm. Samples were mounted on charged slides. After permeabilization (0.2% Triton X-100+ 0.01%
785 Tween 20) and blocking (5% goat serum), cells were incubated overnight with the following primary antibodies: α-
786 SOX2 (Santa Cruz Biotechnology sc-365823; 1:50), α- Tyrosine Hydroxylase (TH; Millipore AB152; 1:1000), α-
787 GFAP (Stemcell Technologies 60048; 1:100), α-IBA-1 (Santa Cruz Biotechnology sc-32725; 1:50), α-Tubulin β 3
788 (Tuj1; Biolegend MMS-435P; 1:200). The appropriate secondary antibody (Alexa Fluor 594 goat anti-rabbit, Alexa
789 Fluor 594 goat anti-mouse, Alexa Fluor 488 goat anti-rabbit, or Alexa Fluor 488 goat anti-mouse) was then added
790 for one hour. Nuclei were counter-stained with DAPI. As an additional quality control measure, H&E staining was
791 also performed on sectioned neurospheres. Fluorescent and brightfield imaging was performed using the BioTek
792 Cytation5 imager fitted with the appropriate filters.

793 **Infection of Neurospheres**

794 **HIV-1 Infection**

795 Differentiated neurospheres were infected with either dual-tropic HIV-1 89.6 (MOI:10; ~250 ng of p24),
796 JR-CSF (MOI:10), or CHO40 (MOI:10) and InfectinTM (Virongy, LLC) (day 0). The total final volume of spheres
797 + virus + Infectin was approximately 200 µL. After 48 hours of incubation (day 2), neurospheres were gently
798 washed with PBS and received fresh differentiation media with or without cART cocktail (lamivudine (NRTI),
799 tenofovir disoproxil fumarate (NRTI), emtricitabine (NRTI), indinavir (protease inhibitor); 2.5 µM each). HIV-1 +
800 cART neurospheres also received treatment with stem cell EVs at an approximate ratio of 1:250 (uninfected
801 recipient cell to EV). HIV-1 89.6 neurospheres received additional cART and EV treatments every two to three
802 days. After a period of seven to fourteen day, neurospheres and supernatants were harvested for downstream
803 analysis. To enrich cytokines from neurosphere supernatants, Nanotrap particles (NT082/NT080; Ceres
804 Nanosciences, Inc.) were used following protocols recently published by our lab [72, 133, 152].

805 **HTLV-1 co-culture**

806 HUT 102 cells (log phase) were cultured in RPMI-1640 supplemented with 10% heat-inactivated,
807 exosome-depleted FBS for 5 days. Cells were then seeded at 1.0 x 10^6 viable cells/mL and exposed to IR using a
808 RS-2000 X-Ray Irradiator (Rad Source Technologies) at a dose of 10 Gy. Irradiated cells were co-cultured with

809 differentiated neurospheres (day 0) at an approximate ratio of 1:100 (infected cells: uninfected cells in neurospheres)
810 with or without combination treatment of interferon-α (10 K unit) and zidovudine (20 μM), hereafter referred to as
811 IFN/AZT. Treatments were added every two to three days and after fourteen days the neurosphere co-cultures were
812 harvested for downstream analysis.

813 **Western Blot**

814 Protein lysates were analyzed via Bradford assay following the manufacturer's recommendations (Bio-
815 Rad). For western blot, equal amounts of protein were mixed with Laemmli buffer, heated at 95°C, and separated
816 on a 4-20% Tris-glycine SDS gel (Invitrogen). Proteins were transferred to an Immobilon PVDF membrane
817 (Millipore) overnight at 50 milliamps. After blocking the membrane with 5% milk in PBS with 0.1% Tween-20, the
818 appropriate primary antibody was added for overnight incubation at 4 °C. Antibodies used for these experiments
819 included α-p24 (NIH AIDS Reagent Program; 1:1000), α-Nef (NIH AIDS Reagent Program; 1:1000), α-Tax (kindly
820 provided by Dr. Scott Gitlin, University of Michigan; 1:1000), α-p19 (Santa Cruz Biotechnology sc-1665; 1:200), α-
821 Integrin αM/CD11b (Santa Cruz Biotechnology sc-515923; 1:200), α-CD163 (Santa Cruz Biotechnology sc-20066;
822 1:200), α- glutamine synthetase (Santa Cruz Biotechnology sc-74430; 1:200), α-GFAP (Santa Cruz Biotechnology
823 sc-166481; 1:200), α-Tyrosine Hydroxylase (Millipore Sigma AB152; 1:200), α-FOXA2 (Santa Cruz Biotechnology
824 sc-101060; 1:200), α-GAD65 (Santa Cruz Biotechnology sc-377145; 1:200), α-GAD67 (Santa Cruz Biotechnology
825 sc-28376; 1:200), α-BNPI (Santa Cruz Biotechnology sc-377425; 1:200), α-SOX2 (Santa Cruz Biotechnology sc-
826 365823; 1:200), α-PARP-1 (Santa Cruz Biotechnology sc-7150; 1:200), α-Caspase 3 (Santa Cruz Biotechnology sc-
827 7148; 1:200), α-BAD (Santa Cruz Biotechnology sc-8044; 1:200), microglia marker sampler panel (α-CD11b, α-
828 CD45, α-IBA-1; Abcam ab226482; 1:1000 each), α-IBA-1 (Santa Cruz Biotechnology sc-32725; 1:200), α-TNFα
829 (Santa Cruz Biotechnology sc-52749; 1:200), α-IL-8 (Santa Cruz Biotechnology sc-376750; 1:200), α-IL-1β (Santa
830 Cruz Biotechnology sc-32294; 1:200) , α-PKR (Santa Cruz Biotechnology sc-136352; 1:200), α-DICER (Cell
831 Signaling Technology 3363S; 1:1000), α-ADAR1 (Santa Cruz Biotechnology sc-271854; 1:200) , α-RIG-I (Santa
832 Cruz Biotechnology sc-376845; 1:200), α-MMP9 (Cell Signaling Technology 2270S; 1:200), α-CD4 (R&D Systems
833 MAB3791; 1:1000), α-CCR5 (R&D Systems MAB1802; 1:000) and α-Actin (Abcam ab-49900; 1:5000).
834 Membranes were subsequently washed, incubated with the appropriate secondary antibody at 4 °C, and then
835 immediately developed using either Clarity or Clarity Max Western ECL Substrate (Bio-Rad). Chemiluminescence

836 imaging was performed with the ChemiDoc Touch Imaging System (Bio-Rad). For reference, all full-length blots
837 are presented in Supplementary Fig. 11.

838 **Reverse Transcription and Quantitative PCR**

839 Total RNA from neurospheres and EVs was extracted using TRIzol reagent (Invitrogen) following the
840 manufacturer's recommendations. Reverse transcription was carried out with the GoScript Reverse Transcription
841 System (Promega) following the manufacturer's recommended protocols. The following specific primers were
842 used: HIV-1 trans-activation response (TAR) reverse primer (5′-CAACAGACGGGCACACACTAC-3′), HIV-1
843 envelope reverse primer: (5′-TGGGATAAGGGTCTGAAACG-3′), HTLV-1 Tax reverse primer (5′-
844 AACACGTAGACTGGGTATCC-3′), HTLV-1 bZIP factor (HBZ) reverse primer (5′-TGACACAGGCAAGCA
845 TCG-3′), HTLV-1 envelope reverse primer (5′-CCATCGTTAGCGCTT CCAGCCCC-3′) [68, 129], AC120498.9
846 reverse primer (5′-TGAAGTCTCGTTCTGTTGCC-3′), ADIRF-AS1 reverse primer (5′-CGGAGTCTTACTCTGTC
847 ATCCA-3′), and GAPDH reverse primer (5′-CAGAGTTAAAAGCAGCCCTGGT-3′).

848 qPCR for HIV-1 TAR and envelope was carried out with IQ Supermix (Bio-Rad). The following
849 primers/probes were used: TAR forward primer (5′-GGTCTCTCTGGTTAGACCAGATCTG-3′), TAR reverse
850 primer (5′-CAACAGACGGGCACACACTAC-3′), TAR Probe (5′-56-FAM-AGCCTCAAT AAAGCTTGCCTTG
851 AGTGCTTC-36-TAMSp-3′). Serially diluted DNA from HIV-1 8E5 cells (NIH AIDS Reagent Program) were
852 included as standards [129]. The reaction conditions were 50°C for 2 minutes (1 cycle), 95 °C for 3 minutes (1
853 cycle), 95 °C for 15 seconds and 60°C for 40 seconds (41 cycles). Quantification was determined from the average
854 cycle threshold (Ct) values of each sample relative to the standard curve. All reactions were run triplicate on the
855 CFX96 Real-Time PCR Detection System (Bio-Rad).

856 qPCR of HTLV-1 Tax, HBZ, and envelope was carried out with SYBR Green Master Mix (Bio-Rad) using
857 the following primers: Tax forward primer (5′- ATCCCGTGGAGACTCCTCAA-3′), Tax reverse primer (5′-
858 AACACGTAGACTGGGTATCC-3′), HBZ forward primer (5′-AGAACGCGA CTCAACCGG-3′), HBZ reverse
859 primer (5′-TGACACAGGCAAGCATCG-3′, Tm), envelope forward primer (5′-CGGGATCCTAGCGTGGGAA
860 CAGGT-3′), envelope reverse primer (5′-CCATCGTTAGCGCTTCCAGCCCC-3′). Serially diluted DNA from
861 HTLV-1 infected cells (HUT 102) served as standards [68]. The reaction conditions were as follows: Tax: 50°C for
862 2 minutes (1 cycle), 95°C for 2 minutes (1 cycle), 95°C for 15 seconds, 51°C for 20 seconds, and 72°C for 40
863 seconds (40 cycles), 65°C for 5 seconds (1 cycle), 95°C for 5 seconds (1 cycle); HBZ: 50°C for 2 minutes (1 cycle),

864 95°C for 2 minutes (1 cycle), 95°C for 15 seconds, 65.7°C for 20 seconds, and 72°C for 40 seconds (40 cycles),
865 65°C for 5 seconds (1 cycle) and 95°C for 5 seconds (1 cycle); envelope: 50°C for 2 minutes (1 cycle), 95°C for 2.5
866 minutes (1 cycle), 95°C for 15 seconds and 64°C for 40 seconds (40 cycles), 65°C for 5 seconds (1 cycle), and 95°C
867 for 5 seconds (1 cycle) [68]. Sample quantification was determined from the average cycle threshold (Ct) values of
868 each sample relative to the standard curve. All reactions were run in triplicate (technical replicates) on the CFX96
869 Real-Time PCR Detection System (Bio-Rad).

870 qPCR of EV-associated lncRNAs was carried out with SYBR Green Master Mix (Bio-Rad) using the
871 following primers: AC120498.9 forward primer (5′-GGTCCTGGGAATCTGCTTT-3′), AC120498.9 reverse primer
872 (5′-GCCTAGCCAACATGGTGAAA-3′), ADIRF-AS1 forward primer (5′-TGCAAT GGCGGGATCTT-3′) and
873 ADIRF-AS1 reverse primer (5′-GTGGCTCATGCCTGTAATCT-3′). qPCR of EV-associated GAPDH was carried
874 out with IQ Supermix (Bio-Rad) using the following primers and probe: GAPDH forward primer (5′-GAAGGTGA
875 AGGTCGGAGTCAA C-3′), GAPDH reverse primer (5′-CAGAGTTAAAAGCAGCCCTGGT-3′), GAPDH probe
876 (5′- /56-FAM/TTTGGT CGTATTGGGCGCCT/36-TAMSp/-3’). The reaction conditions were as follows: 95˚C
877 for 10 minutes (1 cycle), followed by 41 cycles of 95˚C for 15 seconds, 54.8 °C/54.7˚C (depending on primers) for
878 20 seconds, and 72˚C for 10 seconds.

879 All reactions were run in triplicate on the CFX96 Real-Time PCR Detection System (Bio-Rad). Data were
880 normalized to GAPDH and the relative expression levels were evaluated using the $2^{-\Delta\Delta CT}$ method [153].

881 **HIV-1 Integration Assay**

882 DNA was extracted from neurosphere samples and 8E5 (positive control) cells using the Qiagen DNeasy
883 Blood & Tissue Kit following the manufacturer’s protocol. DNA was quantified with the NanoDrop and 100 ng of
884 DNA from each sample was used for the Alu-*Gag* PCR assay. The following primers/probe were used: 1st
885 integration (targeting Alu-*Gag*): Alu forward primer (5′-GCCTCCCAAAGTGCTGGGATTACAG-3′), HIV-*Gag*
886 reverse primer (5′-GTTCCTGCTATGTCACTTCC-3′) [125]; 2nd integration (targeting HIV-1 TAR): TAR forward
887 primer (5′- GGTCTCTCTGGTTAGACCAGATCTG-3′), TAR reverse primer (5′- CAACAGACGGG
888 CACACACTAC-3′), TAR probe (5′-56-FAM-AGCCTCAAT AAAGCTTGCCTTGAGTGCTTC-36-TAMSp-3′)
889 [129]. The reaction conditions for the 1st integration PCR were as follows: 95˚C for 2 minutes (1 cycle), followed
890 by 39 cycles of 95˚C for 15 seconds, 50˚C for 15 seconds, and 72˚C for 3.5 minutes. The reaction conditions for the
891 2nd integration (quantitative) PCR were as follows: 95˚C for 3 minutes (1 cycle), followed by 41 cycles of 95˚C for

892 15 seconds and 60˚C for 40 seconds. Samples were run in triplicate on the CFX96 Real-Time PCR Detection
893 System (Bio-Rad) and Ct values were exported for data analysis.

894 **Isolation and Characterization of EVs**

895 **Stem Cell EVs and A549 EVs**

896 EV isolation was performed as previously described [72]. Briefly, human bone marrow MSCs (BM-
897 MSCs) (ATCC PCS-500-012) and human lung carcinoma cell line A549 (ATCC CCL-185) were cultured in the
898 presence of exosome-depleted FBS (Thermo Fisher Scientific) prior to collection of conditioned medium. Human
899 iPSCs (ATCC ACS-1019), which were cultured in serum-free/xeno-free medium, received full media changes every
900 day and the conditioned medium was collected and stored at 4°C throughout expansion. Bulk conditioned medium
901 was first spun at 2,000 x g and then filtered with a 0.22 µm filter to remove cellular debris and larger vesicles.
902 Filtered medium then underwent concentration and buffer exchange via TFF (Spectrum) to isolate EVs. Samples
903 were subsequently aliquoted and frozen at -20°C for downstream analysis. The size distribution and concentration
904 of each EV sample was assessed via nanoparticle tracking analysis (NTA) using the NanoSight NS300 (Malvern
905 Panalytical). Prior to analysis the equipment was calibrated per the manufacturer's protocols. EV samples were
906 diluted in sterile PBS immediately before measurement. The acquired data was analyzed by the instrument's built-
907 in software.

908 **HIV-1 and Human Coronavirus OC43 EVs**

909 U1 cART EVs were isolated via ultracentrifugation. First, supernatants were centrifuged at 1,200 rpm for
910 five minutes to pellet any cellular debris. The resulting supernatant was then centrifuged at 100,000 x g for 90
911 minutes using the 70Ti rotor (Beckman). The pellet was washed with PBS followed by another centrifugation at
912 100,000 × g for 90 minutes. EV pellets were resuspended in PBS and then frozen at -20°C for downstream analysis.
913 A549 cells were infected with 5.0 x 10^5 TCID50 of human coronavirus OC43 for 96 hours. Supernatants
914 were collected and centrifuged at 2,000 rpm for five minutes, filtered through a 0.22 µm sterile filter, and then
915 centrifuged at 100,000 x g for 90 minutes using the 70Ti rotor (Beckman). The pellet was resuspended in sterile
916 PBS and treated with 45 mJ/cm^3 of UV(C) LED irradiation. Samples of UV(C)-treated EVs (1, 5, 10 µL) were
917 added to Vero cells for two passages and no viral outgrowth was detected (data not shown). Remaining EVs were
918 frozen at -20°C for downstream analysis.

919 U1 cART and OC43 EVs were analyzed via NTA using the ZetaView Z-NTA (Particle Metrix). Prior to
920 analysis the equipment was calibrated per the manufacturer's recommendation and each EV sample was diluted in
921 deionized water prior to analysis. The acquired data was analyzed by the instrument's built-in software.

922 **Transmission Electron Microscopy (negative staining method)**

923 To prepare EV samples for electron microscopy, different dilutions of each sample were prepared and 5 µL
924 was adsorbed to the formvar side of a glow-discharged, 200 mesh copper grid with formvar and carbon coating.
925 Excess sample was removed from the grids with filter paper. Samples were fixed with 4% glutaraldehyde in 0.12 M
926 sodium cacodylate buffer (pH 7.2) for five minutes, washed four times with distilled, deionized water, and stained
927 with 1% aqueous uranyl acetate for 60 seconds. The uranyl acetate was removed with filter paper and allowed to air
928 dry. Imaging was performed using an FEI Talos F200X transmission electron microscope at 80KV (Thermo Fisher
929 Scientific).

930 **EV Uptake**

931 EVs were labeled with either SYTO RNASelect Green Fluorescent Stain (Thermo Fisher) or BODIPY
932 493/503 (Thermo Fisher) following the manufacturer's recommended protocol. Excess dye was removed via
933 centrifugation using a Sephadex G-10 (Sigma-Aldrich) column with a glass wool bottom packed with 0.75 mL
934 beads. Labeled EVs were added to differentiated neurospheres and incubated at 37°C (day 0) at an approximate
935 ratio of 1:250 (uninfected recipient cell to EV ratio). On day 1, neurospheres received a complete media
936 replacement. Neurospheres also received fresh media on days four and seven. Fluorescent imaging was performed
937 using the BioTek Cytation 5 and phase contrast images were taken with a Zeiss Axio Observer.Z1 microscope.

938 **RNA Sequencing and Analysis**

939 Total RNA was extracted from EVs using TRIzol reagent (Invitrogen) following the manufacturer's
940 recommendations. RNA sequencing and sequence analysis was performed by LC Sciences, LLC. Briefly, the 2100
941 Bioanalyzer System (Agilent) was used to analyze total RNA and ribosomal RNA was removed per the Ribo-Zero
942 Gold Kit (Illumina). The remaining RNA fragments were used to construct a strand-specific cDNA library using the
943 dUTP method (average library insert size was 300 ± 50 bp) and pair-end sequencing was performed using the Hiseq
944 4000 (Illumina) following the manufacturer's recommended protocol. Reads containing adaptor contamination and
945 low quality bases were removed with Cutadapt and in-house perl scripts [154]. FastQC was used to verify transcript

946 quality, Tophat2 [155] and Bowtie 2 [156] were used for mapping reads to the genome, and in-house Perl scripts
947 were used for GO and KEGG enrichment analysis. StringTie [157] was used for transcript assembly and Ballgown
948 [158] was used to perform differential expression analysis. Significant terms for GO analysis were determined by a
949 hypergeometric equation and GO terms with a p value <0.05 were considered significant [159]. All data generated
950 from the RNAseq analysis represents data from one biological replicate each of A549, MSC, and iPSC EVs.
951 The secondary structures of selected long non-coding RNAs were predicted using the RNAfold Server of
952 the ViennaRNA Websuite [160]. RNA sequences were first retrieved from NCBI and the FASTA sequence was
953 submitted to the server. This server predicted the minimum free energy (mfe) secondary structure of single
954 sequences using a programming algorithm originally developed by Zuker and Stiegler [161]. The secondary
955 structures were predicted using a temperature setting of 37 °C and keeping all other parameters to default [162].

956 **Immunoprecipitation for direct PCR**

957 Neurospheres were washed with PBS and treated with 0.25% Trypsin/EDTA (diluted 1:1 with PBS) for
958 three to five minutes at 37°C. Trypsin was neutralized by the addition of RPMI-1640 with 10% FBS. The
959 appropriate antibodies (α-CD11b (Santa Cruz Biotechnology sc-515923; 1:200); α-GFAP (Santa Cruz
960 Biotechnology sc-166481; 1:200), αGAD-65 (Santa Cruz Biotechnology sc-377145; 1:200), α-SOX2 (Santa Cruz
961 Biotechnology sc-365823; 1:200)) were added (5 µg per 10E5 cells) and incubated at 4°C for four hours on a
962 rotator. Protein A+G washed beads (30 µL; 30% slurry in PBS with 0.01% BSA) were added to the cell/antibody
963 mixture and incubated for 1.5 hours at 4°C. Samples were spun at 1,000g for five minutes, washed once with
964 PBS/BSA buffer, and pellets (protein A/G beads + cells + antibody in ~25µl packed beads) were resuspended in
965 PBS (20 µL). Approximately 1/5 of the solution was used for direct PCR. The first cycle of PCR (heat for strand
966 separation) is sufficient to crack open viruses and eukaryotic cells. An initial titration of an astrocyte cell line with
967 antibody and beads was used to titrate the amount of beads/cell/antibody needed for direct PCR using GAPDH
968 primers (data not shown).

969 **RNA Pull-down**

970 The following RNA sequences were synthesized with 5' Biotin conjugates: UAGCUGGGAUUACAG
971 GCGUGCACCACCACACCCGGCUAAUUUUUGUAUUUUU (AC120498.9) and CUCACUGCAACCUCU
972 GCCUUCCAGGUUCAA (ADIRF-AS1). Whole cell lysate (SHSY5Y, CCF-STTG-1, or MDM) (approximately 75

973 μg) was incubated with approximately 10 μg of each biotinylated RNA overnight at 4°C. The next day,
974 Streptavidin-Sepharose beads (BioVision) were added and again incubated at 4°C for an additional two hours. The
975 samples were spun at 14000 x g and resuspended in TNE50 + 0.1% NP40. Samples were mixed with Laemmli
976 buffer for subsequent SDS/PAGE and western blot was performed for PKR, DICER, ADAR1, and RIG-I (as
977 described above).

978 **Cell Viability Assay**

979 SHYSY5Y cells were seeded in a 96-well plate (day 0). On day one, cells were treated with either U1
980 cART EVs (1:50,000 approximate recipient cell to EV ratio) or OC43 EVs (1:6,500 approximate recipient cell to
981 EV ratio) to induce damage. Stem cell EVs were treated with 45 mJ/cm3 of UV(C) LED irradiation to inactivate
982 EV-associated RNA. Stem cell EVs were subsequently added at an approximate ratio of 1:1000 (recipient cell to
983 EV ratio). Untreated cells received PBS. Each sample was performed in triplicate. Cells were observed daily. On
984 day eight representative photographs were taken using an EVOS XL microscope and viability was assayed using the
985 CellTiter-Glo Luminescent Cell Viability kit (Promega) per the manufacturer's protocol. Luminescence was
986 measured with the GloMax Multi Detection System (Promega).

987 **Zymography**

988 EVs were added to a 30% slurry of NT80/82 Nanotrap particles (Ceres Biosciences) and PBS was added to
989 bring the final volume to 500 μL. Samples were rotated at 4°C for two hours, spun, and washed with PBS.
990 Laemmli buffer was added to each sample, heated for ten minutes at 37°C, and then spun to pellet the Nanotraps.
991 The resulting supernatants were loaded on a Novex 10% Zymogram Plus (Gelatin) Protein Gel (ThermoFisher
992 Scientific). The gel was run at 120V for approximately 90 minutes, renatured for 30 minutes at room temperature
993 on a rocker, and incubated at 37°C in developing buffer for a period of 24 to 36 hours. After development, the gel
994 was gently stained for an additional 24 to 48 hours with Coomassie blue R-250. Imaging was performed with the
995 ChemiDoc Touch Imaging System (Bio-Rad).

996 **Statistical Analysis**

997 Analysis of quantitative data was performed by using Graph Pad Prism. The *P* values were determined via
998 analysis of variance (ANOVA) using multiple comparisons. To justify the use of ANOVA, experimental data was

assumed to approximate a normal distribution. *P* values were defined as follows: of greatest statistical significance (< 0.0001), of greater significance (< 0.005), and significant (< 0.05).

Acknowledgements

We would like to thank all members of the Kashanchi lab for their contributions, especially Gwen Cox and interns Gabrielle Heller and Sahan Raghavan. We also would like express thanks to ATCC management, especially Drs. Mindy Goldsborough and James Kramer for supporting this work. This work was further supported by National Institutes of Health (NIH) Grants AI078859, AI074410, AI127351-01, AI043894, and NS099029 (to FK), R21DA050176 and R01NS099029 (to FK and LAL), and R33 CA206937 and R01AR068436 (to LAL). The content is solely the responsibility of the authors and does not necessarily represent the official views of the National Institutes of Health. Targeted Pharmaceuticals, LLC partially funded experiments related to 3D cultures and HIV-1 infections.

Author Contributions

H.B. wrote and edited the manuscript. D.Y. and S.J. contributed to development, characterization, and production of iPSCs and NPCs. H.B. contributed to the production of EVs and C.A.B. contributed to EV analysis. H.B., P.K., S.A.S., M.C., Y.K., J.E. carried out experiments and contributed to data analysis. L.A.L. and N.E. contributed to the experimental designs. F.K. contributed to the overall direction and coordination of the study as well as contributions to experimental design and data analysis.

Competing Interests

H.B, D.Y., and S.J. are employed by ATCC and L.A.L. is affiliated with Ceres Nanosciences, Inc. All other authors declare no potential conflicts of interest.

1025 **References**

1026 1. UNAIDS. Global HIV & AIDS statistics — 2019 fact sheet. PDF at
1027 https://www.unaids.org/sites/default/files/media_asset/UNAIDS_FactSheet_en.pdf.

1028 2. Saylor, D., *et al*. HIV-associated Neurocognitive Disorder--Pathogenesis and Prospects for Treatment. *Nat Rev*
1029 *Neurol*. **12**, 234-48 (2016).

1030 3. Chen, M.F., Gill, A.J., Kolson, D.L. Neuropathogenesis of HIV-associated Neurocognitive Disorders: Roles for
1031 Immune Activation, HIV Blipping and Viral Tropism. *Curr Opin HIV AIDS*. **9**, 559-64 (2014).

1032 4. Eggers, C., *et al*. HIV-1-associated Neurocognitive Disorder: Epidemiology, Pathogenesis, Diagnosis, and
1033 Treatment. *J Neurol*. **264**, 1715-1727 (2017).

1034 5. Ferrell, D. & Giunta, B. The Impact of HIV-1 on Neurogenesis: Implications for HAND. *Cell Mol Life Sci*. **71**,
1035 4387-92 (2014).

1036 6. Rao, V.R., Ruiz, A.P., Prasad, V.R. Viral and Cellular Factors Underlying Neuropathogenesis in HIV Associated
1037 Neurocognitive Disorders (HAND). *AIDS Res Ther*. **19**, 11:13 (2014).

1038 7. Ru, W. & Tang, S.J. HIV-associated Synaptic Degeneration. *Mol Brain*. **10**, 40 (2017).

1039 8. Teodorof-Diedrich, C. & Spector, S.A. Human Immunodeficiency Virus Type 1 gp120 and Tat Induce
1040 Mitochondrial Fragmentation and Incomplete Mitophagy in Human Neurons. *J Virol*. **92**, e00993-18 (2018).

1041 9. Kaushik, A., Jayant, R.D., Bhardwaj, V., Nair, M. Personalized Nanomedicine for CNS Diseases. *Drug Discov*
1042 *Today*. **23**, 1007-1015 (2018).

1043 10. GBD 2016 Neurology Collaborators. Global, Regional, and National Burden of Neurological Disorders, 1990-
1044 2016: A Systematic Analysis for the Global Burden of Disease Study 2016. *Lancet Neurol*. **18**, 459-480 (2019).

1045 11. Shi, Y., Inoue, H., Wu, J.C., Yamanaka, S. Induced Pluripotent Stem Cell Technology: A Decade of Progress.
1046 *Nat Rev Drug Discov*. **16**, 115-130 (2017).

1047 12. Takahashi, K. & Yamanaka, S. Induction of Pluripotent Stem Cells From Mouse Embryonic and Adult
1048 Fibroblast Cultures by Defined Factors. *Cell*. **126**, 663-76 (2006).

1049 13. Takahashi, K., *et al*. Induction of Pluripotent Stem Cells From Adult Human Fibroblasts by Defined Factors.
1050 *Cell*. **131**, 861-72 (2007).

1051 14. Hu, B.Y., Du, Z.W., Zhang, S.C. Differentiation of Human Oligodendrocytes From Pluripotent Stem Cells.
1052 *Nat Protoc*. **4**, 1614-22 (2009).

1053 15. Haston, K.M. & Finkbeiner, S. Clinical Trials in a Dish: The Potential of Pluripotent Stem Cells to Develop
1054 Therapies for Neurodegenerative Diseases. *Annu Rev Pharmacol Toxicol*. **56**, 489-510 (2016).

1055 16. Abud, E.M., *et al*. iPSC-Derived Human Microglia-like Cells to Study Neurological Diseases. *Neuron*. **94**,
1056 278-293 (2017).

1057 17. de Rus Jacquet, A. Preparation and Co-Culture of iPSC-Derived Dopaminergic Neurons and Astrocytes. *Curr*
1058 *Protoc Cell Biol*. **85**, e98 (2019).

1059 18. Lanko, K., *et al*. Replication of the Zika Virus in Different iPSC-derived Neuronal Cells and Implications to
1060 Assess Efficacy of Antivirals. *Antiviral Res*. **145**, 82-86 (2017).

1061 19. Fujimori, K., *et al*. Modeling Sporadic ALS in iPSC-derived Motor Neurons Identifies a Potential Therapeutic
1062 Agent. *Nat Med*. **24**, 1579-1589 (2018).

1063 20. Lebedeva, O.S. & Lagarkova, M.A. Pluripotent Stem Cells for Modelling and Cell Therapy of Parkinson's
1064 Disease. *Biochemistry (Mosc)*. **83**, 1046-1056 (2018).

1065 21. Monzio Compagnoni, G., *et al*. Mitochondrial Dysregulation and Impaired Autophagy in iPSC-Derived
1066 Dopaminergic Neurons of Multiple System Atrophy. *Stem Cell Reports*. **11**, 1185-1198 (2018).

1067 22. Huang, B., *et al*. Inflammatory Responses to a Pathogenic West Nile Virus Strain. *BMC Infect Dis*. **19**, 912
1068 (2019).

1069 23. Penney, J., Ralvenius, W.T., Tsai, L.H. Modeling Alzheimer's Disease With iPSC-derived Brain Cells. *Mol*
1070 *Psychiatry*. **25**, 148-167 (2020).

1071 24. Csobonyeiova, M., Polak, S., Danisovic, L. Recent Overview of the Use of iPSCs Huntington's Disease
1072 Modeling and Therapy. *Int J Mol Sci*. **21**, 2239 (2020).

1073 25. Teque, F., *et al*. Genetically-edited Induced Pluripotent Stem Cells Derived From HIV-1-infected Patients on
1074 Therapy Can Give Rise to Immune Cells Resistant to HIV-1 Infection. *AIDS*. **34**, 1141-114 (2020).

1075 26. Pampaloni, F., Reynaud, E.G., Stelzer, E.H. The Third Dimension Bridges the Gap Between Cell Culture and
1076 Live Tissue. *Nat Rev Mol Cell Biol*. **8**, 839-45 (2007).

1077 27. Topol, A., Tran, N.N., Brennand, K.J. A Guide to Generating and Using hiPSC Derived NPCs for the Study of
1078 Neurological Diseases. *J Vis Exp*. **96**, e52495 (2015).

1079 28. Zhou, S., *et al*. Neurosphere Based Differentiation of Human iPSC Improves Astrocyte Differentiation. *Stem*
1080 *Cells Int*. **2016**, 4937689 (2016).

1081 29. Hofrichter, M., *et al*. Comparative Performance Analysis of Human iPSC-derived and Primary Neural
1082 Progenitor Cells (NPC) Grown as Neurospheres in Vitro. *Stem Cell Res*. **25**, 72-82 (2017).

1083 30. Ostenfeld, T., *et al*. Regional Specification of Rodent and Human Neurospheres. *Brain Res Dev Brain Res*.
1084 **134**, 43-55 (2002).

1085 31. Parmar, M., Skogh, C., Björklund, A., Campbell, K. Regional Specification of Neurosphere Cultures Derived
1086 From Subregions of the Embryonic Telencephalon. *Mol Cell Neurosci*. **21**, 645-56 (2002).

1087 32. Jensen, J.B. & Parmar, M. Strengths and limitations of the neurosphere culture system. *Mol Neurobiol*. **34**,
1088 153-161 (2006).

1089 33. Garcez, P.P., *et al*. Zika virus impairs growth in human neurospheres and brain organoids. *Science.* **352**, 816-
1090 818 (2016).

1091 34. Garcez, P.P., *et al*. Zika virus disrupts molecular fingerprinting of human neurospheres. *Sci Rep*. **7**, 40780
1092 (2017).

1093 35. D'Aiuto, L., *et al*. Generation of three-dimensional human neuronal cultures: application to modeling CNS viral
1094 infections. *Stem Cell Res Ther*. **9**, 134 (2018).

1095 36. Dos Reis, R.S., Sant, S., Keeney, H., Wagner, M.C.E., Ayyavoo, V. Modeling HIV-1 neuropathogenesis using
1096 three-dimensional human brain organoids (hBORGs) with HIV-1 infected microglia. *Sci Rep*. **10**, 15209 (2020).

1097 37. Gribkoff, V.K. & Kaczmarek, L.K. The need for new approaches in CNS drug discovery: Why drugs have
1098 failed, and what can be done to improve outcomes. *Neuropharmacology*. **120**, 11-19 (2017).

1099 38. Danon, J.J., Reekie, T.A., Kassiou, M. Challenges and Opportunities in Central Nervous System Drug
1100 Discovery. *Trends in Chemistry*. **1**, P612-624 (2019).

1101 39. Phinney, D.G. & Pittenger, M.F. Concise Review: MSC-Derived Exosomes for Cell-Free Therapy. *Stem Cells*.
1102 **35**, 851-858 (2017).

1103 40. van Niel, G., D'Angelo, G., Raposo, G. Shedding light on the cell biology of extracellular vesicles. *Nat Rev*
1104 *Mol Cell Biol*. **19**, 213-228 (2018).

1105 41. Zaborowski, M.P., Balaj, L., Breakefield, X.O., Lai, C.P. Extracellular Vesicles: Composition, Biological
1106 Relevance, and Methods of Study. *Bioscience*. **65**, 783-797 (2015).

1107 42. Deng, H., *et al*. Lipid, Protein, and MicroRNA Composition Within Mesenchymal Stem Cell-Derived
1108 Exosomes. *Cell Reprogram*. **20**, 178-186 (2018).

1109 43. Luarte, A., Bátiz, L.F., Wyneken, U., Lafourcade, C. Potential Therapies by Stem Cell-Derived Exosomes in
1110 CNS Diseases: Focusing on the Neurogenic Niche. *Stem Cells Int*. **2016**, 5736059 (2016).

1111 44. Taheri, B., *et al*. Induced pluripotent stem cell-derived extracellular vesicles: A novel approach for cell-free
1112 regenerative medicine. *J Cell Physiol*. **234**, 8455-8464 (2019).

1113 45. Koniusz, S., *et al*. Extracellular Vesicles in Physiology, Pathology, and Therapy of the Immune and Central
1114 Nervous System, with Focus on Extracellular Vesicles Derived from Mesenchymal Stem Cells as Therapeutic
1115 Tools. *Front Cell Neurosci*. **10**, 109 (2016).

1116 46. Keshtkar, S., Azarpira, N., Ghahremani, M.H. Mesenchymal stem cell-derived extracellular vesicles: novel
1117 frontiers in regenerative medicine. *Stem Cell Res Ther*. **9**, 63 (2018).

1118 47. Branscome, H., *et al*. Use of Stem Cell Extracellular Vesicles as a "Holistic" Approach to CNS Repair. *Front*
1119 *Cell Dev Biol*. **8**, 455 (2020).

1120 48. Galieva, L.R., James, V., Mukhamedshina, Y.O., Rizvanov, A.A. Therapeutic Potential of Extracellular
1121 Vesicles for the Treatment of Nerve Disorders. *Front Neurosci*. **13**, 163 (2019).

1122 49. Mesci, P., *et al*. Blocking Zika virus vertical transmission. *Sci Rep*. **8**, 1218 (2018).

1123 50. Ye, L., *et al*. Blood cell-derived induced pluripotent stem cells free of reprogramming factors generated by
1124 Sendai viral vectors. *Stem Cells Transl Med*. **2**, 558-566 (2013).

1125 51. D'Aiuto, L., *et al*. Large-scale generation of human iPSC-derived neural stem cells/early neural progenitor cells
1126 and their neuronal differentiation. *Organogenesis*. **10**, 365-377 (2014).

1127 52. Chandrasekaran, A., *et al*. Comparison of 2D and 3D neural induction methods for the generation of neural
1128 progenitor cells from human induced pluripotent stem cells. *Stem Cell Res*. **25**, 139-151 (2017).

1129 53. Kang, S., *et al*. Characteristic analyses of a neural differentiation model from iPSC-derived neuron according to
1130 morphology, physiology, and global gene expression pattern. *Sci Rep*. **7**, 12233 (2017).

1131 54. Bianchi, F., *et al*. Rapid and efficient differentiation of functional motor neurons from human iPSC for neural
1132 injury modelling. *Stem Cell Res*. **32**, 126-134 (2018).

1133 55. Simão, D., *et al*. Recapitulation of Human Neural Microenvironment Signatures in iPSC-Derived NPC 3D
1134 Differentiation. *Stem Cell Reports*. **11**, 552-564 (2018).

1135 56. Blumberg, B.M., Gelbard, H.A., Epstein, L.G. HIV-1 infection of the developing nervous system: central role
1136 of astrocytes in pathogenesis. *Virus Res*. **32**, 253-267 (1994).

1137 57. Gray, L.R., *et al*. Is the central nervous system a reservoir of HIV-1?. *Curr Opin HIV AIDS*. **9**, 552-558
1138 (2014).

1139 58. Li, G.H., Henderson L., Nath, A. Astrocytes as an HIV Reservoir: Mechanism of HIV Infection. *Curr HIV*
1140 *Res*. **14**, 373-381 (2016).

1141 59. Joseph, S.B., Arrildt, K.T., Sturdevant, C.B., Swanstrom, R. HIV-1 target cells in the CNS. *J Neurovirol*. **21**,
1142 276-289 (2015).

1143 60. Rojas-Celis, V., Valiente-Echeverría, F., Soto-Rifo, R., Toro-Ascuy, D. New Challenges of HIV-1 Infection:
1144 How HIV-1 Attacks and Resides in the Central Nervous System. *Cells*. **8**, 1245 (2019).

1145 61. Wallet, C., *et al*. Microglial Cells: The Main HIV-1 Reservoir in the Brain. *Front Cell Infect Microbiol*. **9**, 362
1146 (2019).

1147 62. Lutgen, V., *et al*. HIV infects astrocytes in vivo and egresses from the brain to the periphery. *PLoS Pathog*.
1148 **16**, e1008381 (2020).

1149 63. Haenseler, W., *et al*. A Highly Efficient Human Pluripotent Stem Cell Microglia Model Displays a Neuronal-
1150 Co-culture-Specific Expression Profile and Inflammatory Response. *Stem Cell Reports*. **8**, 1727-1742 (2017).

1151 64. McQuade, A., Coburn, M., Tu, C.H., Hasselmann, J., Davtyan, H., Blurton-Jones, M. Development and
1152 validation of a simplified method to generate human microglia from pluripotent stem cells. *Mol Neurodegener*. **13**,
1153 67 (2018).

1154 65. Jaworski, E., *et al*. The use of Nanotrap particles technology in capturing HIV-1 virions and viral proteins from
1155 infected cells. *PLoS One*. **9**, e96778 (2014).

1156 66. Levin, M.C. & Jacobson, S. HTLV-I associated myelopathy/tropical spastic paraparesis (HAM/TSP): a chronic
1157 progressive neurologic disease associated with immunologically mediated damage to the central nervous system. *J*
1158 *Neurovirol*. **3**,126-140 (1997).

1159 67. Grant, C., *et al*. Human T cell leukemia virus type I and neurologic disease: events in bone marrow, peripheral
1160 blood, and central nervous system during normal immune surveillance and neuroinflammation. *J Cell Physiol*. **190**,
1161 133-59 (2002).

1162 68. Lepoutre, V., Jain, P., Quann, K., Wigdahl, B., Khan, Z.K. Role of resident CNS cell populations in HTLV-1-
1163 associated neuroinflammatory disease. *Front Biosci (Landmark Ed)*. **14**, 1152-1168 (2009).

1164 69. Nozuma, S. & Jacobson, S. Neuroimmunology of Human T-Lymphotropic Virus Type 1-Associated
1165 Myelopathy/Tropical Spastic Paraparesis. *Front Microbiol*. **10**, 885 (2019).

1166 70. Iordanskiy, S., *et al*. Therapeutic doses of irradiation activate viral transcription and induce apoptosis in HIV-1
1167 infected cells. *Virology*. **485**, 1-15 (2015).

1168 71. Iordanskiy, S. & Kashanchi, F. Potential of Radiation-Induced Cellular Stress for Reactivation of Latent HIV-1
1169 and Killing of Infected Cells. *AIDS Res Hum Retroviruses*. **32**,120-124 (2016).

1170 72. Pinto, D.O., *et al*. HTLV-1 Extracellular Vesicles Promote Cell-to-Cell Contact. *Front Microbiol*. **10**, 2147
1171 (2019).

1172 73. Gill, P.S., *et al*. Treatment of adult T-cell leukemia-lymphoma with a combination of interferon alfa and
1173 zidovudine. *N Engl J Med*. **332**, 1744-1748 (1995).

1174 74. Hermine, O., *et al*. Brief report: treatment of adult T-cell leukemia-lymphoma with zidovudine and interferon
1175 alfa. *N Engl J Med*. **332**, 1749-1751 (1995).

1176 75. Pasquier, A., *et al*. How to Control HTLV-1-Associated Diseases: Preventing de Novo Cellular Infection Using
1177 Antiviral Therapy. *Front Microbiol*. **9**, 278 (2018).

1178 76. Branscome, H., *et al*. Stem Cell Extracellular Vesicles and their Potential to Contribute to the Repair of
1179 Damaged CNS Cells. *J Neuroimmune Pharmacol.* **15**, 520-537 (2020).

1180 77. Heinemann, M.L. & Vykoukal, J. Sequential Filtration: A Gentle Method for the Isolation of Functional
1181 Extracellular Vesicles. *Methods Mol Biol*. **1660**, 33-41 (2017).

1182 78. Busatto, S., *et al*. Tangential Flow Filtration for Highly Efficient Concentration of Extracellular Vesicles from
1183 Large Volumes of Fluid. *Cells*. **7**, 273 (2018).

1184 79. Haraszti, R.A., *et al*. Exosomes Produced from 3D Cultures of MSCs by Tangential Flow Filtration Show
1185 Higher Yield and Improved Activity. *Mol Ther*. **26**, 2838-2847 (2018).

1186 80. El Baradie, K.B.Y., *et al*. Freeze-Dried Extracellular Vesicles From Adipose-Derived Stem Cells Prevent
1187 Hypoxia-Induced Muscle Cell Injury. *Front Cell Dev Biol*. **8**, 181 (2020).

1188 81. Larsen, P.H., Wells, J.E., Stallcup, W.B., Opdenakker, G., Yong, V.W. Matrix metalloproteinase-9 facilitates
1189 remyelination in part by processing the inhibitory NG2 proteoglycan. *J Neurosci*. **23**, 11127-11135 (2003).

1190 82. Reinhard, S.M., Razak, K., Ethell, I.M. A delicate balance: role of MMP-9 in brain development and
1191 pathophysiology of neurodevelopmental disorders. *Front Cell Neurosci*. **9**, 280 (2015).

1192 83. Toth, M. & Fridman, R. Assessment of Gelatinases (MMP-2 and MMP-9 by Gelatin Zymography. *Methods*
1193 *Mol Med*. **57**, 163-174 (2001).

1194 84. Tajhya, R.B., Patel, R.S., Beeton, C. Detection of Matrix Metalloproteinases by Zymography. *Methods Mol*
1195 *Biol*. **1579**, 231-244 (2017).

1196 85. Chang, C.L., *et al*. Adipose-derived mesenchymal stem cell-derived exosomes markedly protected the brain
1197 against sepsis syndrome induced injury in rat. *Am J Transl Res*. **11**, 3955-3971 (2019).

1198 86. Kumar, P., *et al*. Neuroprotective effect of placenta-derived mesenchymal stromal cells: role of exosomes.
1199 *FASEB J*. **33**, 5836-5849 (2019).

1200 87. Liu, W., *et al*. Exosomes Derived from Bone Mesenchymal Stem Cells Repair Traumatic Spinal Cord Injury by
1201 Suppressing the Activation of A1 Neurotoxic Reactive Astrocytes. *J Neurotrauma*. **36**, 469-484 (2019).

1202 88. Guo, H., *et al*. Bone marrow mesenchymal stem cells-derived exosomes improve injury of hippocampal
1203 neurons in rats with depression by upregulating microRNA-26a expression. *Int Immunopharmacol*. **82**, 106285
1204 (2020).

1205 89. Chen, H.X., *et al*. Exosomes derived from mesenchymal stem cells repair a Parkinson's disease model by
1206 inducing autophagy. *Cell Death Dis*. **11**, 288 (2020).

1207 90. Liu, C.Y., *et al*. Effect of exosomes from adipose-derived stem cells on the apoptosis of Schwann cells in
1208 peripheral nerve injury. *CNS Neurosci Ther*. **26**, 189-196 (2020).

1209 91. Long, Q., *et al*. Intranasal MSC-derived A1-exosomes ease inflammation, and prevent abnormal neurogenesis
1210 and memory dysfunction after status epilepticus. *Proc Natl Acad Sci U S A*. **114**, E3536-E3545 (2017).

1211 92. Ding, M., *et al*. Exosomes Isolated From Human Umbilical Cord Mesenchymal Stem Cells Alleviate
1212 Neuroinflammation and Reduce Amyloid-Beta Deposition by Modulating Microglial Activation in Alzheimer's
1213 Disease. *Neurochem Res*. **43**, 2165-2177 (2018).

1214 93. Feng, N., Jia, Y., Huang, X. Exosomes from adipose-derived stem cells alleviate neural injury caused by
1215 microglia activation via suppressing NF-kB and MAPK pathway. *J Neuroimmunol*. **334**, 576996 (2019).

1216 94. Ni, H., *et al*. Exosomes Derived From Bone Mesenchymal Stem Cells Ameliorate Early Inflammatory
1217 Responses Following Traumatic Brain Injury. *Front Neurosci*. **13**, 14 (2019).

1218 95. Sun, G., *et al*. hucMSC derived exosomes promote functional recovery in spinal cord injury mice via
1219 attenuating inflammation. *Mater Sci Eng C Mater Biol Appl*. **89**, 194-204 (2018).

1220 96. Thomi, G., Surbek, D., Haesler, V., Joerger-Messerli, M., Schoeberlein, A. Exosomes derived from umbilical
1221 cord mesenchymal stem cells reduce microglia-mediated neuroinflammation in perinatal brain injury. *Stem Cell Res*
1222 *Ther*. **10**, 105 (2019).

1223 97. Ching, R.C., Wiberg, M., Kingham, P.J. Schwann cell-like differentiated adipose stem cells promote neurite
1224 outgrowth via secreted exosomes and RNA transfer. *Stem Cell Res Ther*. **9**, 266 (2018).

1225 98. Qiu, G., *et al.* Mesenchymal stem cell-derived extracellular vesicles affect disease outcomes via transfer of
1226 microRNAs. *Stem Cell Res Ther*. **9**, 320 (2018).

1227 99. Bodart-Santos, V., *et al*. Extracellular vesicles derived from human Wharton's jelly mesenchymal stem cells
1228 protect hippocampal neurons from oxidative stress and synapse damage induced by amyloid-β oligomers. *Stem Cell*
1229 *Res Ther*. **10**, 332 (2019).

1230 100. Yin, K., Wang, S. Zhao, R.C. Exosomes from mesenchymal stem/stromal cells: a new therapeutic paradigm.
1231 *Biomark Res*. **7**, 8 (2019).

1232 101. Shojaati, G., *et al*. Mesenchymal Stem Cells Reduce Corneal Fibrosis and Inflammation via Extracellular
1233 Vesicle-Mediated Delivery of miRNA. *Stem Cells Transl Med*. **8**, 1192-1201 (2019).

1234 102. Baglio, S.R., *et al*. Human bone marrow- and adipose-mesenchymal stem cells secrete exosomes enriched in
1235 distinctive miRNA and tRNA species. *Stem Cell Res Ther*. **6**, 127 (2015).

1236 103. Ferguson, S.W., *et al*. The microRNA regulatory landscape of MSC-derived exosomes: a systems view. *Sci*
1237 *Rep*. **8**, 1419 (2018).

1238 104. Kaur, S., *et al*. Small non-coding RNA landscape of extracellular vesicles from human stem cells. *Sci Rep*. **8**,
1239 15503 (2018).

1240 105. Cole, J.L. Activation of PKR: an open and shut case? *Trends Biochem Sci*. **32**, 57-62 (2007).

1241 106. Husain, B., Mukerji, I., Cole, J.L. Analysis of high-affinity binding of protein kinase R to double-stranded
1242 RNA. *Biochemistry*. **51**, 8764-8770 (2012).

1243 107. Narayanan, A., *et al*. Exosomes derived from HIV-1-infected cells contain trans-activation response element
1244 RNA. *J Biol Chem*. **288**, 20014-33 (2013).

1245 108. Sampey, G.C., *et al*. Exosomes from HIV-1-infected Cells Stimulate Production of Pro-inflammatory
1246 Cytokines through Trans-activating Response (TAR) RNA. *J Biol Chem*. **291**, 1251-1266 (2016).

1247 109. Barclay, R.A., *et al*. Exosomes from uninfected cells activate transcription of latent HIV-1. *J Biol Chem*.
1248 **292**, 14764 (2017).

1249 110. Barclay, R.A., *et al*. An Omics Approach to Extracellular Vesicles from HIV-1 Infected Cells. *Cells*. **8**, 787
1250 (2019).

1251 111. Rai, M.A., Hammonds, J., Pujato, M., Mayhew, C., Roskin, K., Spearman, P. Comparative analysis of human
1252 microglial models for studies of HIV replication and pathogenesis. *Retrovirology*. **17**, 35 (2020).

1253 112. Roberts, E.S., Masliah, E., Fox, H.S. CD163 identifies a unique population of ramified microglia in HIV
1254 encephalitis (HIVE). *J Neuropathol Exp Neurol*. **63**, 1255-1264 (2004).

1255 113. Korzhevskii, D.E. & Kirik, O.V. Brain Microglia and Microglial Markers. *Neurosci Behav Physi*. **46**, 284-
1256 290 (2016).

1257 114. Hopperton, K.E., Mohammad, D., Trépanier, M.O., Giuliano, V., Bazinet, R.P. Markers of microglia in post-
1258 mortem brain samples from patients with Alzheimer's disease: a systematic review. *Mol Psychiatry*. **23**, 177-198
1259 (2018).

1260 115. Zrzavy, T., *et al*. Pro-inflammatory activation of microglia in the brain of patients with sepsis. *Neuropathol*
1261 *Appl Neurobiol*. **45**, 278-290 (2019).

1262 116. DePaula-Silva, A.B., *et al*. Differential transcriptional profiles identify microglial- and macrophage-specific
1263 gene markers expressed during virus-induced neuroinflammation. *J Neuroinflammation*. **16**, 152 (2019).

1264 117. Guillemin, G.J. & Brew, B.J. Microglia, macrophages, perivascular macrophages, and pericytes: a review of
1265 function and identification. *J Leukoc Biol*. **75**, 388-397 (2004).

1266 118. Kaul, M., Zheng, J., Okamoto, S., Gendelman, H.E., Lipton, S.A. HIV-1 infection and AIDS: consequences
1267 for the central nervous system. *Cell Death Differ*. **12 Suppl 1**, 878-892 (2005).

1268 119. Nuovo, G.J. & Alfieri, M.L. AIDS dementia is associated with massive, activated HIV-1 infection and
1269 concomitant expression of several cytokines. *Mol Med*. **2**, 358-366 (1996).

1270 120. Bagasra, O., *et al*. Cellular reservoirs of HIV-1 in the central nervous system of infected individuals:
1271 identification by the combination of in situ polymerase chain reaction and immunohistochemistry. *AIDS*. **10**, 573-
1272 585 (1996).

1273 121. Takahashi, K., *et al*. Localization of HIV-1 in human brain using polymerase chain reaction/in situ
1274 hybridization and immunocytochemistry. *Ann Neurol*. **39**, 705-711 (1996).

1275 122. Chompre, G., *et al*. Astrocytic expression of HIV-1 Nef impairs spatial and recognition memory. *Neurobiol*
1276 *Dis*. **49**, 128-136 (2013).

1277 123. O'Doherty, U., Swiggard, W.J., Jeyakumar, D., McGain, D., Malim, M.H. A sensitive, quantitative assay for
1278 human immunodeficiency virus type 1 integration. *J Virol*. **76**, 10942-10950 (2002).

1279 124. Yu, J.J., *et al*. A more precise HIV integration assay designed to detect small differences finds lower levels of
1280 integrated DNA in HAART treated patients. *Virology*. **379**, 78-86 (2008).

1281 125. Liszewski, M.K., Yu, J.J., O'Doherty, U. Detecting HIV-1 integration by repetitive-sampling Alu-gag PCR.
1282 *Methods*. **47**, 254-260 (2009).

1283 126. Pinzone, M.R. & O'Doherty, U. Measuring integrated HIV DNA ex vivo and in vitro provides insights about
1284 how reservoirs are formed and maintained. *Retrovirology*. **15**, 22 (2018).

1285 127. Eng, L.F., Ghirnikar, R.S., Lee, Y.L. Glial fibrillary acidic protein: GFAP-thirty-one years (1969-2000).
1286 *Neurochem Res*. **25**, 1439-1451 (2000).

1287 128. Sofroniew, M.V. & Vinters, H.V. Astrocytes: biology and pathology. *Acta Neuropathol*. **119**, 7-35 (2010).

1288 129. Zhou, B.Y., Liu, Y., Kim, Bo, Xiao, Y., He, J.J. Astrocyte activation and dysfunction and neuron death by
1289 HIV-1 Tat expression in astrocytes. *Mol Cell Neurosci*. **27**, 296-305 (2004).

1290 130. Bell, J.E., Anthony, I.C., Simmonds, P. Impact of HIV on regional & cellular organisation of the brain. *Curr*
1291 *HIV Res*. **4**, 249-257 (2006).

1292 131. Zou, W., *et al*. Involvement of p300 in constitutive and HIV-1 Tat-activated expression of glial fibrillary
1293 acidic protein in astrocytes. *Glia*. **58**, 1640-1648 (2010).

1294 132. Teyssier, F., Bay, J.O., Dionet, C., Verrelle, P. Régulation du cycle cellulaire des cellules exposées aux
1295 radiations ionisantes [Cell cycle regulation after exposure to ionizing radiation]. *Bull Cancer*. **86**, 345-357 (1999).

1296 133. DeMarino, C., *et al*. Antiretroviral Drugs Alter the Content of Extracellular Vesicles from HIV-1-Infected
1297 Cells. *Sci Rep*. **8**, 7653 (2018).

1298 134. Pleet, M.L., *et al*. Ebola Virus VP40 Modulates Cell Cycle and Biogenesis of Extracellular Vesicles. *J Infect*
1299 *Dis*. **218 (suppl_5)**, S365-S387 (2018).

1300 135. DeMarino, C., *et al*. Purification of High Yield Extracellular Vesicle Preparations Away from Virus. *J Vis*
1301 *Exp*. **151**, 10.3791/59876 (2019).

1302 136. Gorabi, A.M., *et al*. The Therapeutic Potential of Mesenchymal Stem Cell-Derived Exosomes in Treatment of
1303 Neurodegenerative Diseases. *Mol Neurobiol*. **56**, 8157-8167 (2019).

1304 137. Kaufmann, S.H., Desnoyers, S., Ottaviano, Y., Davidson, N.E., Poirier, G.G. Specific proteolytic cleavage of
1305 poly(ADP-ribose) polymerase: an early marker of chemotherapy-induced apoptosis. *Cancer Res*. **53**, 3976-3985
1306 (1993).

1307 138. Soldani, C. & Scovassi, A.I. Poly(ADP-ribose) polymerase-1 cleavage during apoptosis: an update. *Apoptosis*.
1308 **7**, 321-328 (2002).

1309 139. Kale, J., Osterlund, E., Andrews, D. BCL-2 family proteins: changing partners in the dance towards death.
1310 *Cell Death Differ.* **25**, 65-80 (2018).

1311 140. Cohen, G.M. Caspases: the executioners of apoptosis. *Biochem J*. **326 (Pt 1)(Pt 1)**, 1-16 (1997).

1312 141. Porter, A.G. & Jänicke, R.U. Emerging roles of caspase-3 in apoptosis. *Cell Death Differ*. **6**, 99-104 (1999).

1313 142. Zhang, J., *et al*. Exosome and exosomal microRNA: trafficking, sorting, and function. *Genomics Proteomics*
1314 *Bioinformatics*. **13**, 17-24 (2015).

1315 143. Hewson, C., Capraro, D., Burdach, J., Whitaker, N., Morris, K.V. Extracellular vesicle associated long non-
1316 coding RNAs functionally enhance cell viability. *Noncoding RNA Res*. **1**, 3-11 (2016).

1317 144. Yu, X., Odenthal, M., Fries, J.W. Exosomes as miRNA Carriers: Formation-Function-Future. *Int J Mol Sci*.
1318 **17**, 2028 (2016).

1319 145. Kelemen, E., Danis, J., Göblös, A., Bata-Csörgő, Z., Széll, M. Exosomal long non-coding RNAs as
1320 biomarkers in human diseases. *EJIFCC*. **30**, 224-236 (2019).

1321 146. Abramowicz, A. & Story, M.D. The Long and Short of It: The Emerging Roles of Non-Coding RNA in Small
1322 Extracellular Vesicles. *Cancers (Basel)*. **12**, 1445 (2020).

1323 147. Groot, M. & Lee, H. Sorting Mechanisms for MicroRNAs into Extracellular Vesicles and Their Associated
1324 Diseases. *Cells*. **9**, 1044 (2020).

1325 148. Santer, L., Bär, C., Thum, T. Circular RNAs: A Novel Class of Functional RNA Molecules with a Therapeutic
1326 Perspective. *Mol Ther*. **27**, 1350-1363 (2019).

1327 149. Zhong, Y., *et al*. Circular RNAs function as ceRNAs to regulate and control human cancer progression. *Mol*
1328 *Cancer*. **17**, 79 (2018).

1329 150. Ali, S.A., *et al*. Genetic characterization of HIV type 1 Nef-induced vesicle secretion. *AIDS Res Hum*
1330 *Retroviruses*. **26**, 173-192 (2010).

1331 151. Urbanelli, L., *et al*. The Role of Extracellular Vesicles in Viral Infection and Transmission. *Vaccines (Basel)*.
1332 **7**, 102 (2019).

1333 152. Pinto, D.O., *et al*. Extracellular vesicles from HTLV-1 infected cells modulate target cells and viral spread.
1334 *Retrovirology*. **18**, 6 (2021).

1335 153. Livak, K.J. & Schmittgen, T.D. Analysis of relative gene expression data using real-time quantitative PCR
1336 and the 2(-Delta Delta C(T)) Method. *Methods*. **25**, 402-8 (2001).

1337 154. Martin, M. Cutadapt removes adapter sequences from high-throughput sequencing reads. *EMBnet.journal*.
1338 **17.1** (2011).

1339 155. Kim, D., *et al*. TopHat2: accurate alignment of transcriptomes in the presence of insertions, deletions and gene
1340 fusions. **Genome Biol. 14**, R36 (2013).

1341 156. Langmead, B. & Salzberg, S.L. Fast gapped-read alignment with Bowtie 2. *Nat Methods*. **9**, 357-359 (2012).

1342 157. Pertea, M., *et al*. StringTie enables improved reconstruction of a transcriptome from RNA-seq reads. *Nat*
1343 *Biotechnol*. **33**, 290-295 (2015).

1344 158. Frazee, A.C., *et al*. Ballgown bridges the gap between transcriptome assembly and expression analysis. *Nat*
1345 *Biotechnol*. **33**, 243-246 (2015).

1346 159. Robinson, M. D., McCarthy, D. J., Smyth, G. K. edgeR: a Bioconductor package for differential expression
1347 analysis of digital gene expression data. *Bioinformatics.* **26**, 139–140 (2010).

1348 160. Gruber, A.R., Lorenz, R., Bernhart, S.H., Neuböck, R., Hofacker, I.L. The Vienna RNA websuite. *Nucleic*
1349 *Acids Res*. **36(Web Server issue)**, W70-W74 (2008).

1350 161. Zuker, M. & Stiegler, P. Optimal computer folding of large RNA sequences using thermodynamics and
1351 auxiliary information. *Nucleic Acids Res*. **9**, 133-148 (1981).

1352 162. Mathews, D.H., Sabina, J., Zuker, M., Turner, D.H. Expanded sequence dependence of thermodynamic
1353 parameters improves prediction of RNA secondary structure. *J Mol Biol.* **288**, 911-940 (1999).

1354
1355
1356
1357
1358
1359
1360
1361
1362
1363
1364
1365
1366
1367
1368
1369
1370
1371
1372

1373 **Figure Legends**

1374 **Figure 1. Generation and characterization of NPC-derived neurospheres. (a)** General workflow and
1375 approximate timeline associated with the development of neurospheres using human somatic cells as the starting
1376 material. Figure created with BioRender.com. **(b)** Representative phase contrast images show the appearance and
1377 morphology of NPC-derived neurospheres during the course of the two week differentiation period (weeks 12
1378 through 14). n=3. Scale bar = 100 µm. **(c)** Average diameter (µm) of NPC-derived neurospheres (two
1379 measurements per sphere) during the course of the differentiation period. n=3 neurospheres. **(d)** After the two week
1380 differentiation period (weeks 12 through 14), ICC staining was carried out on differentiated, cross-sectioned
1381 neurospheres. Nuclei were counter-stained with DAPI. Representative images show the relative expression of
1382 NPCs (SOX2), neurons (TH), astrocytes (GFAP), and microglia-like cells (IBA-1). Scale bar= 200 µm. n = 2 for
1383 ICC imaging.

1384 **Figure 2. HIV-1 infection of NPC-derived neurospheres.** Differentiated neurospheres were exposed to dual-
1385 tropic HIV-1 89.6, JR-CSF, or CHO40 (MOI:10). **(a)** Western blot was performed to examine the relative
1386 expression of Pr55, p24, and Nef in HIV-1 89.6 neurospheres cultured with or without cART (lamivudine, tenofovir
1387 disoproxil fumarate, emtricitabine, indinavir) after fourteen days. **(b)** RT-qPCR was performed to examine the
1388 relative copy numbers of TAR and *env* RNA in HIV-1 89.6 neurospheres with or without cART after fourteen days.
1389 n=3. ***$p < 0.0001$. **(c)** Western blot was performed to compare the relative expression of p24 in HIV-1 89.6, JR-
1390 CSF, and CHO40 infected neurospheres after seven days. **(d)** Neurospheres were gently disaggregated and
1391 immunoprecipitation was performed using antibodies specific for astrocytes (GFAP), microglia-like cells (CD11b),
1392 neurons (GAD65), and NSCs (SOX2) followed by direct PCR to quantify copies of TAR DNA in different
1393 cellular subpopulations of HIV-1 89.6, JR-CSF, and CHO40-infected neurospheres. n=3. * $p < 0.05$, ***$p <$
1394 0.0001. Differentiated neurospheres were treated with IL-34 (100 ng/mL), M-CSF (25 ng/mL), TGFβ-1 (50 ng/mL)
1395 every other day for a period of seven days and were then exposed to dual tropic HIV-1 89.6 for a period of fourteen
1396 days with or without cART (lamivudine, tenofovir disoproxil fumarate, emtricitabine, indinavir). **(e)** Western blot
1397 was performed to examine the relative expression of viral proteins (Pr55, p24, Nef), microglia markers (IBA-1,
1398 CD11b, CD45), and apoptotic proteins (PARP-1, BAD). **(f)** RT-qPCR was performed to quantify the relative copy
1399 numbers of TAR and *env* RNA. n=3. *** $p < 0.0001$.

1400 **Figure 3. HTLV-1 co-culture and expression of cellular markers in HIV-1 and HTLV-1 infected**
1401 **neurospheres. (a)** Differentiated neurospheres were exposed to dual-tropic HIV-1 89.6 with or without cART
1402 (lamivudine, tenofovir disoproxil fumarate, emtricitabine, indinavir), or were co-cultured with irradiated HTLV-1
1403 infected cells with or without IFN/AZT for a period of fourteen days. Western blot was performed to examine the
1404 relative expression of various CNS-relevant cellular markers including those associated with microglia-like cells,

1405 astrocytes, neurons (dopaminergic, GABAergic, glutamatergic), and NSCs. **(b)** Western blot was performed to
1406 examine the relative expression of Tax and p19 in neurospheres co-cultured with HTLV-1 infected cells with or
1407 without IFN/AZT treatment. **(c)** RT-qPCR was performed to quantify the copy numbers of *tax*, *env*, and *hbz* RNA
1408 in neurospheres co-cultured with HTLV-1 infected cells with or without IFN/AZT treatment. n=3. ** $p < 0.005$,
1409 *** $p < 0.0001$.

1410 **Figure 4. EV characterization and uptake assay.** EVs from stem cells (MSCs, iPSCs) as well as A549 cancer
1411 cells were concentrated using TFF. Data from A549 EVs is included to serve as a control for NTA analysis and EV
1412 uptake. **(a)** NTA was performed and representative histograms from three independent measurements show the
1413 relative size distribution of each EV prep. **(b)** TEM (negative staining method). EVs were fixed with 4%
1414 glutaraldehyde in 0.12 M sodium cacodylate buffer and stained with 1% aqueous uranyl acetate. Imaging was
1415 performed using an FEI Talos F200X transmission electron microscope at 80KV. Scale bar = 200 nm. **(c)** EVs
1416 were fluorescently labeled with BODIPY 493/503. After removal of excess dye, EVs were added to differentiated
1417 neurospheres (day 0) at an approximate ratio of 1:250 (recipient cell to EV ratio). After 24 hours the media was
1418 completely replaced. Representative brightfield and fluorescent images show the relative uptake of EVs on days 2
1419 and 8. Scale bar = 200 µm. n= 3. **(d)** Phase contrast images show the relative size and morphology of EV-treated
1420 neurospheres after two weeks in culture. Scale bar = 100 µm. n = 3. **(e)** The average diameter (two measurements
1421 per sphere) of EV-treated neurospheres was measured using calibrated imaging software. n = 3 neurospheres.
1422 *** $p < 0.0001$ relative to untreated.

1423 **Figure 5. The effect of EVs on HIV-1 infected neurospheres.** Differentiated neurospheres were exposed to dual-
1424 tropic HIV-1 89.6 with or without cART (lamivudine, tenofovir disoproxil fumarate, emtricitabine, indinavir) for a
1425 period of fourteen days. Additionally, the HIV-1 + cART treated samples were treated with either iPSC, MSC, or
1426 A549 EVs at an approximate ratio of 1:250 (recipient cell to EV ratio). **(a)** Western blot was performed on
1427 neurosphere lysates to evaluate the relative expression of PARP-1, Caspase-3, and BAD. **(b)** Western blot was
1428 performed on neurosphere supernatants to evaluate the relative expression of TNFα, IL-8, and IL-1β.

1429 **Figure 6. RNA analysis of EVs**. RNA sequencing of EV-associated lncRNAs was performed. **(a)** Percentages of
1430 transcripts mapping to either exons, introns, or intergenic regions are shown. **(b)** Percentages of non-annotated
1431 transcripts. Transcripts not annotated in genome databases were designated as novel transcripts according to the
1432 following class codes: i = transfrag falling within a reference intron; j = potentially novel isoform with at least one
1433 splice junction shared with a reference transcript; o = generic exonic overlap with a reference transcript; u =
1434 unknown intergenic transcript; x = exonic overlap with reference on the opposite strand. **(c)** Volcano plots
1435 displaying the differentially expressed transcripts between iPSC and A549 EVs (left panel) and MSC and A549 EVs
1436 (right panel).

1437 Significantly regulated transcripts are annotated with their corresponding gene ID.

1438 **Figure 7. RNA pulldown assay. (a)** The secondary structures of lncRNAs ADIRF-AS1 and AC120498.9
1439 are shown. These lncRNAs contained continuous stretches of dsRNA ≥ 30 base pairs in length; for reference, the
1440 corresponding regions are enclosed in black boxes. **(b)** Total RNA was isolated from EVs and RT-qPCR was
1441 carried out using primers that were specific to the boxed sequences shown in panel a. Data were normalized to
1442 GAPDH and the relative expression levels were evaluated using the $2^{-\Delta\Delta CT}$ method. n = 3. * $p < 0.05$, *** $p <$
1443 0.0001. **(c)** Biotin-conjugated synthetic RNA sequences corresponding to the sequences of interest were incubated
1444 with SHSY5Ywhole cell extract. Western blot was performed to assess the expression of different RNA binding
1445 proteins (PKR, Dicer, ADAR1). **(d)** SHSY5Y cells were exposed to EVs from cART-treated, HIV-1 infected cells
1446 (U1) with or without treatment of stem cell EVs at an approximate ratio of 1:1000 (recipient cell to EV ratio). Stem
1447 cell EVs were exposed to UV(C) to inactivate EV-associated RNAs. Representative images show the appearance
1448 and morphology of cells after 8 days in culture. Inserts are included for higher resolution. Scale bar = 200 µm. n =
1449 3. **(e)** Cell viability was quantified via CellTiter-Glo. n=3. * $p < 0.05$ relative to U1 cART EVs.

a)

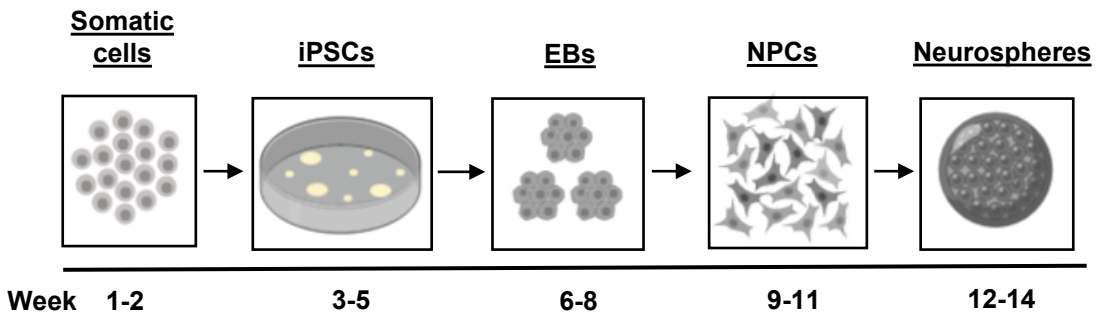

b)

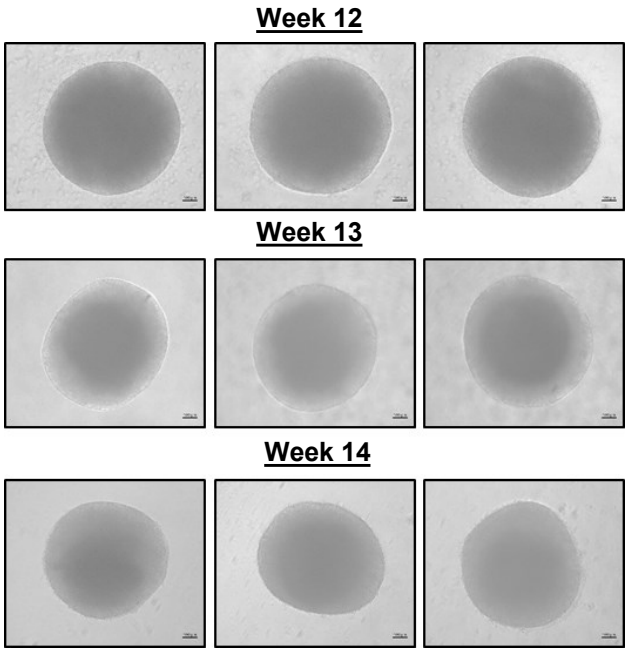

c)

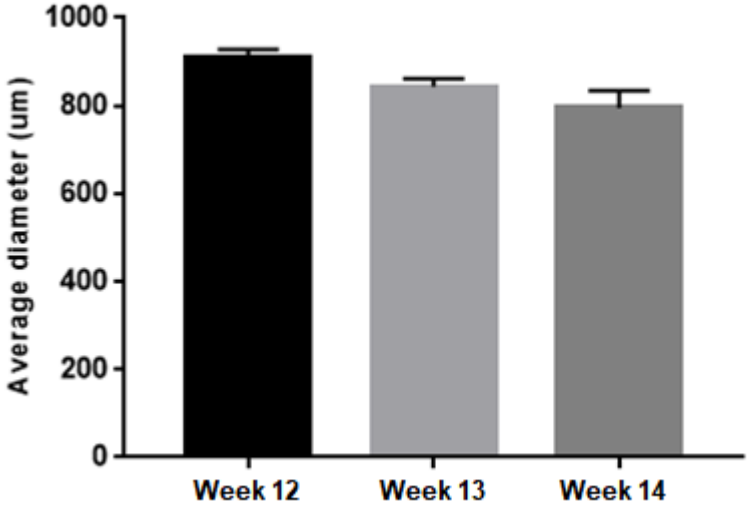

Branscome et al. Fig. 1a-c

d)

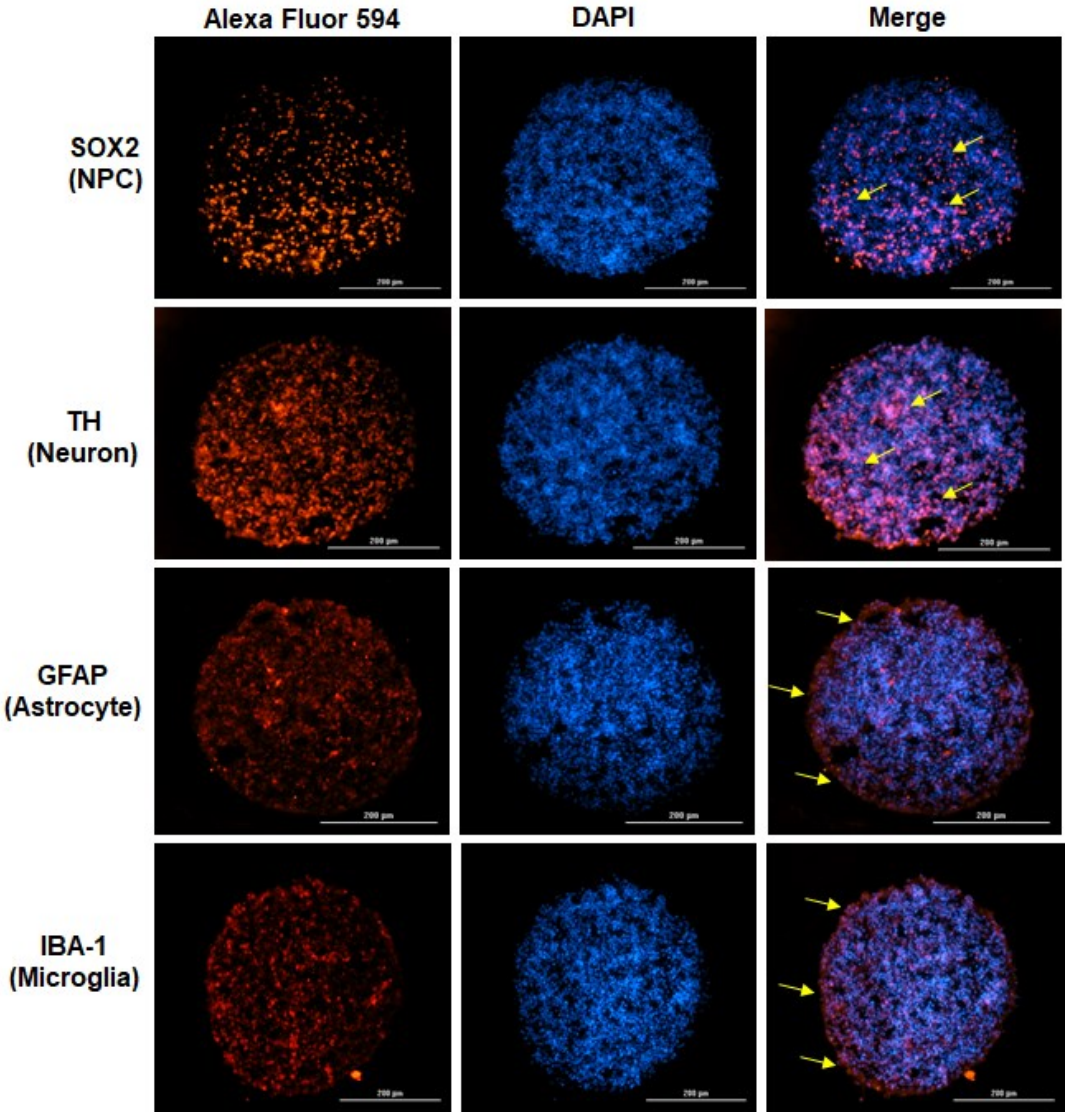

Branscome et al. Fig. 1d

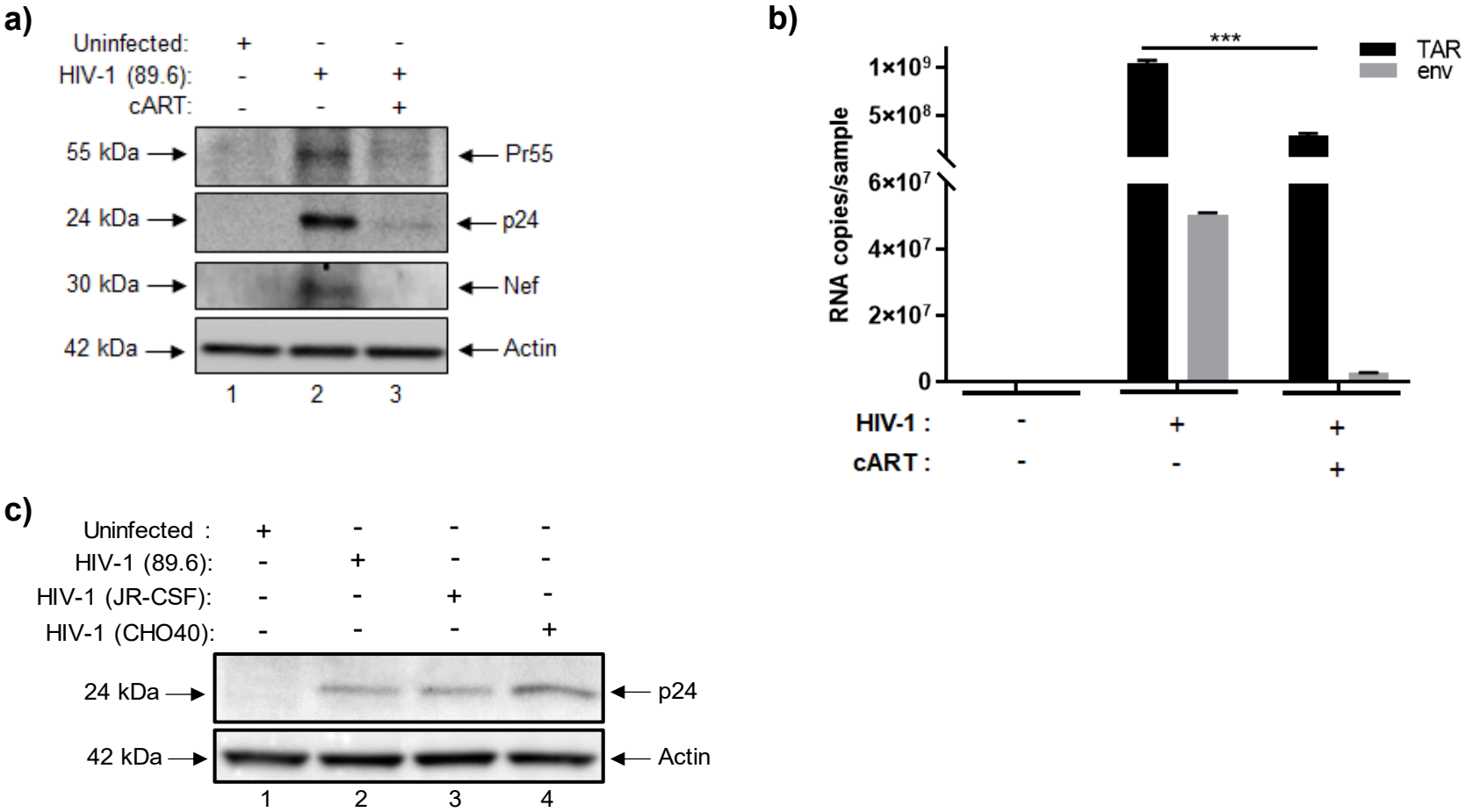

Branscome et al. Fig. 2a-c

d)

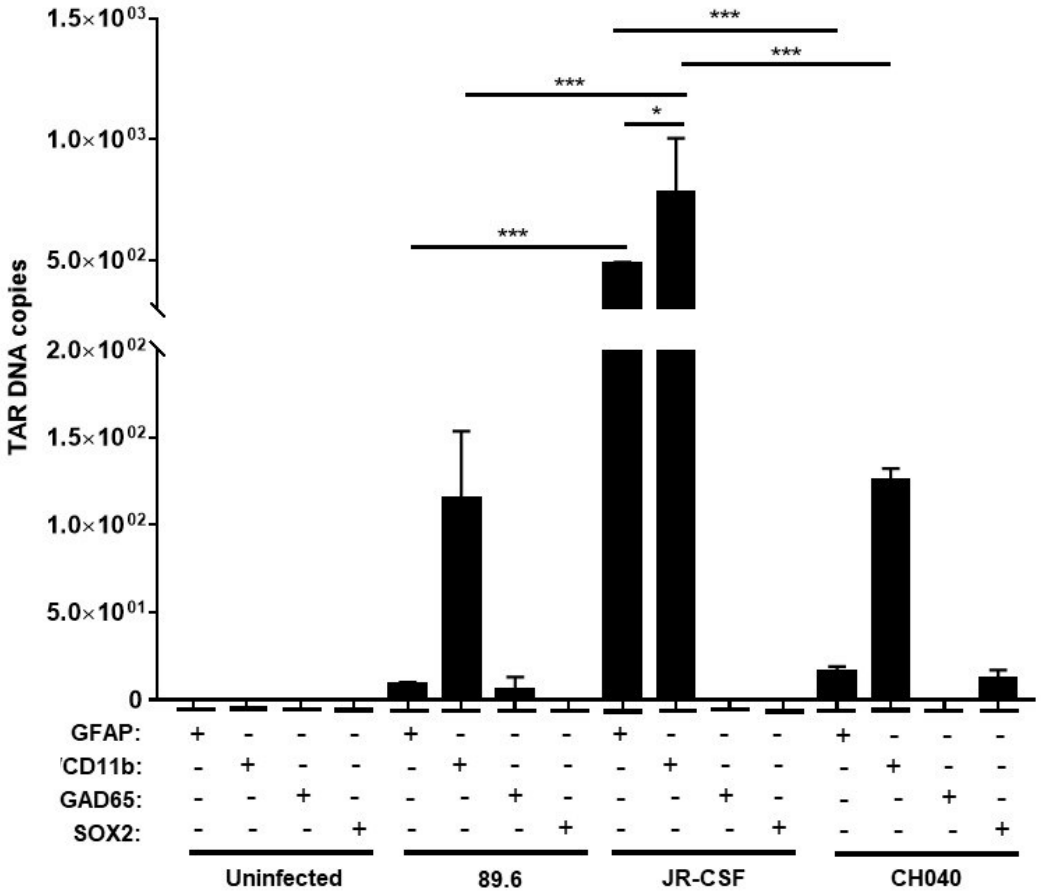

Branscome et al. Fig. 2d

e)

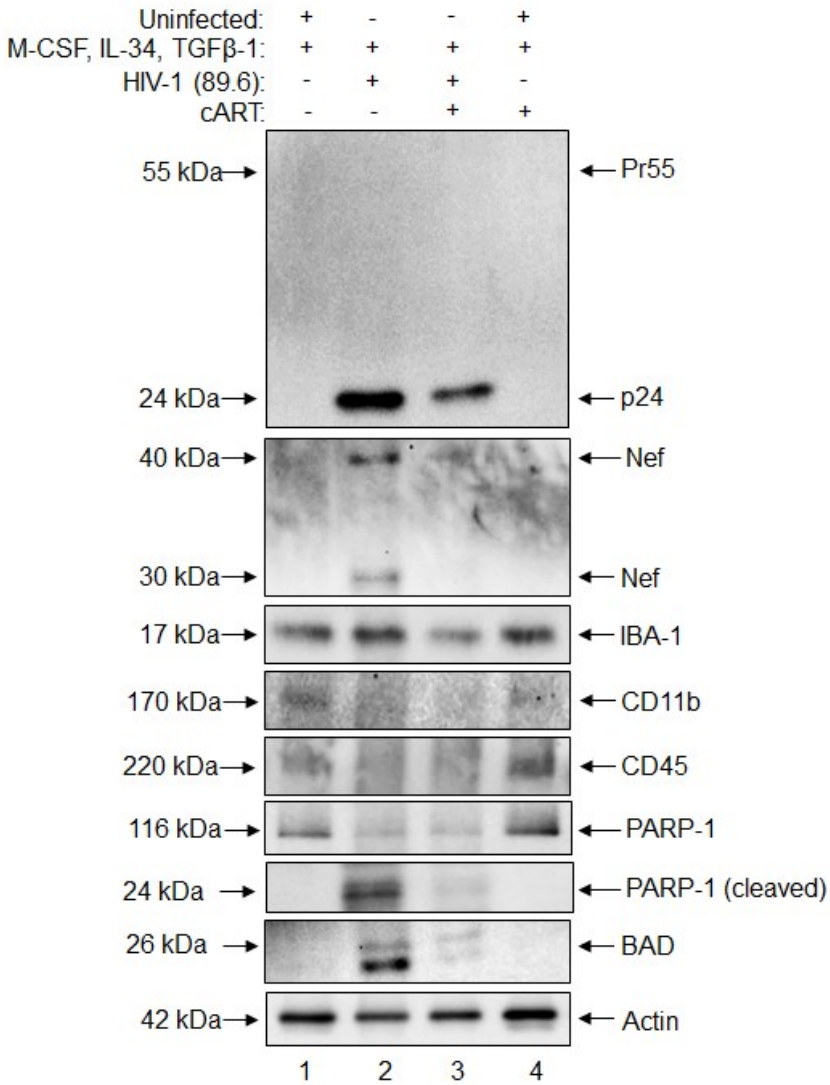

f)

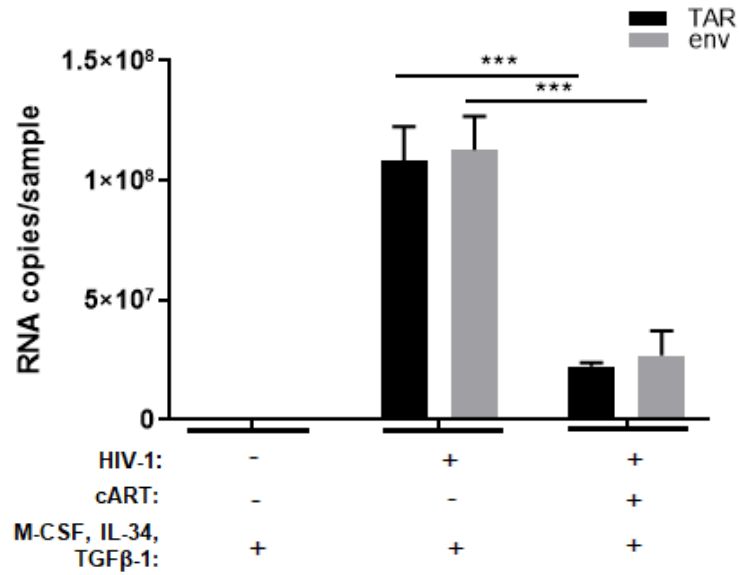

Branscome et al. Fig. 2e-f

a)

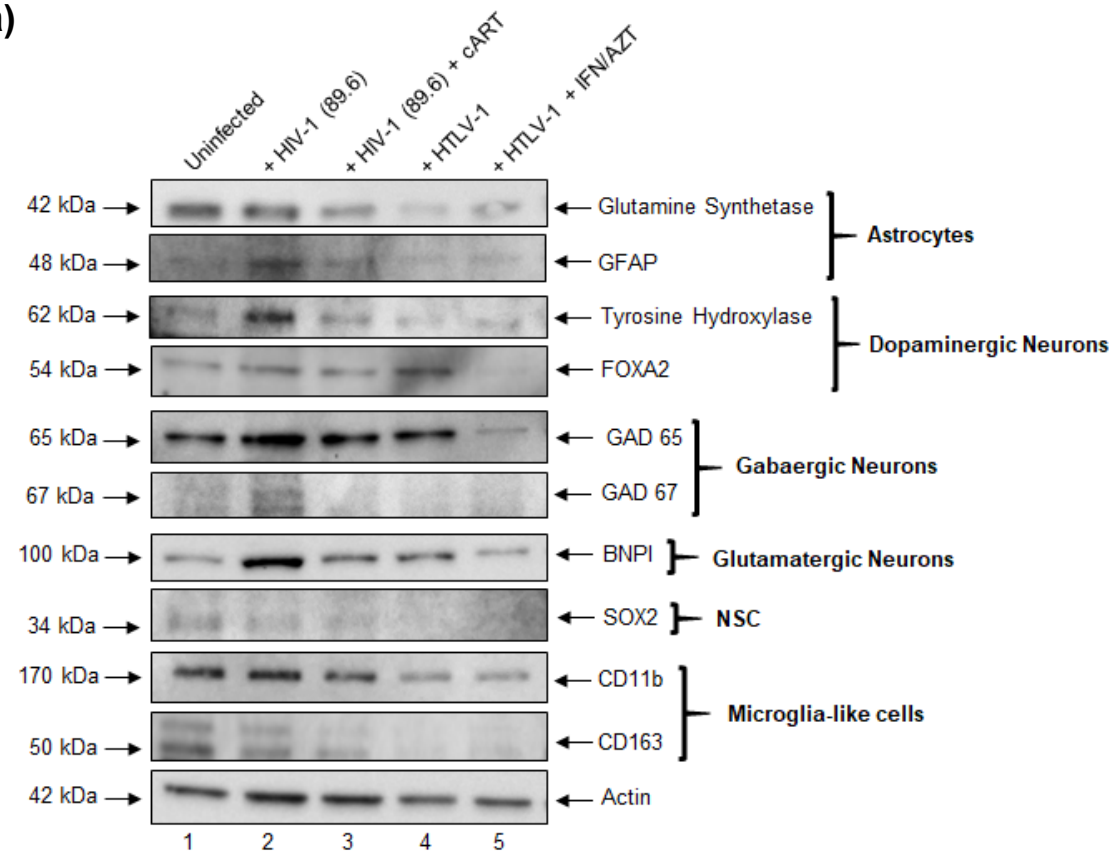

Branscome et al. Fig. 3a

b)

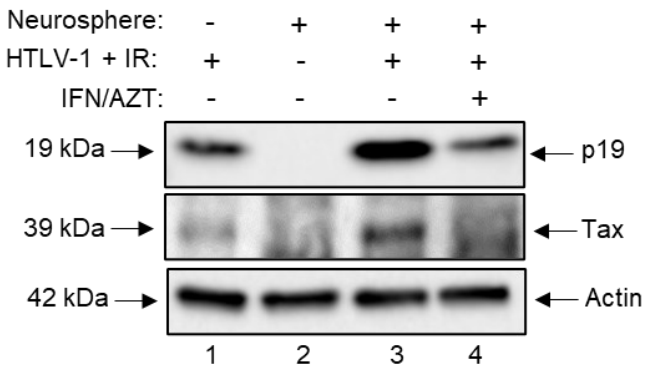

c)

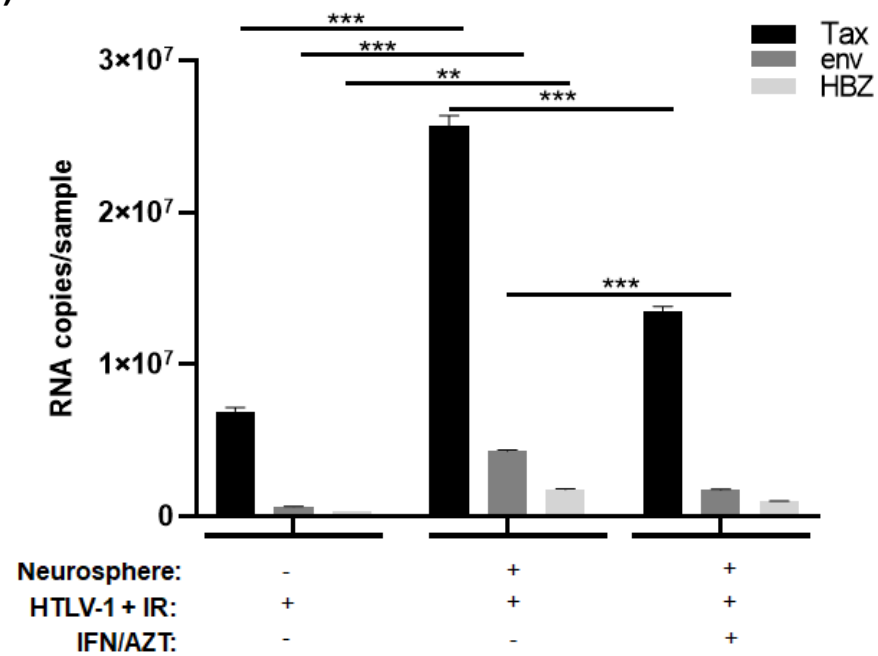

Branscome et al. Fig. 3b-c

a)

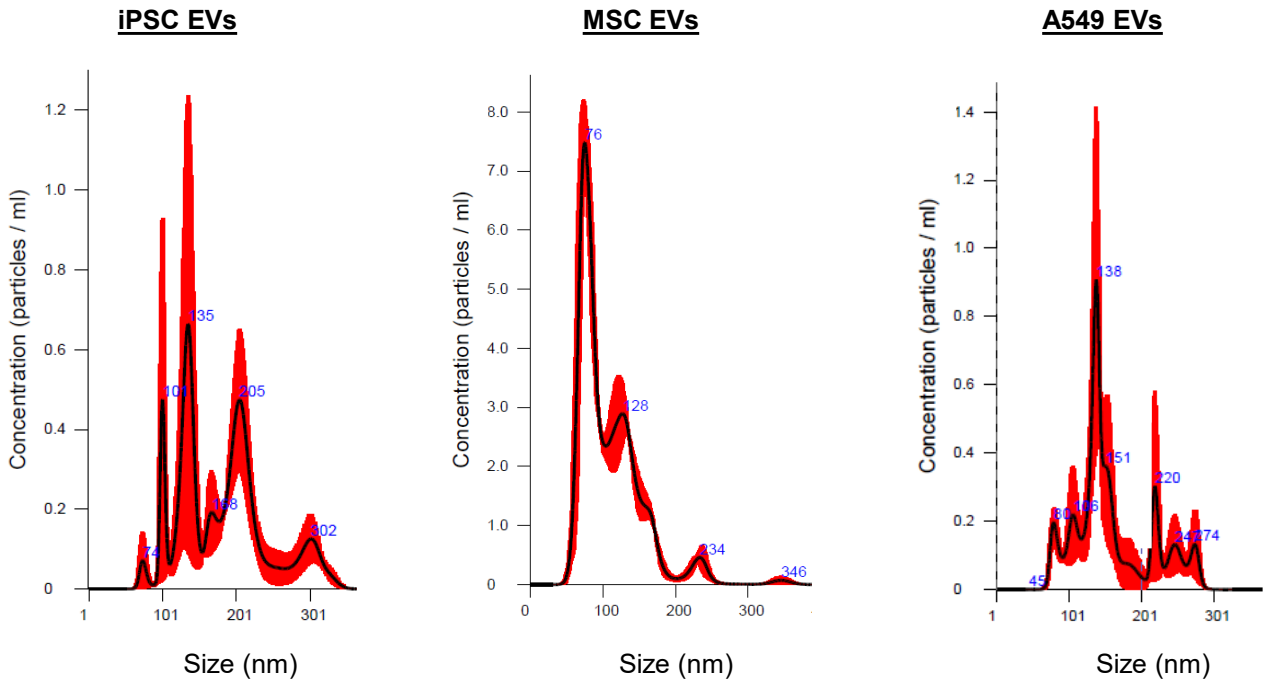

b)

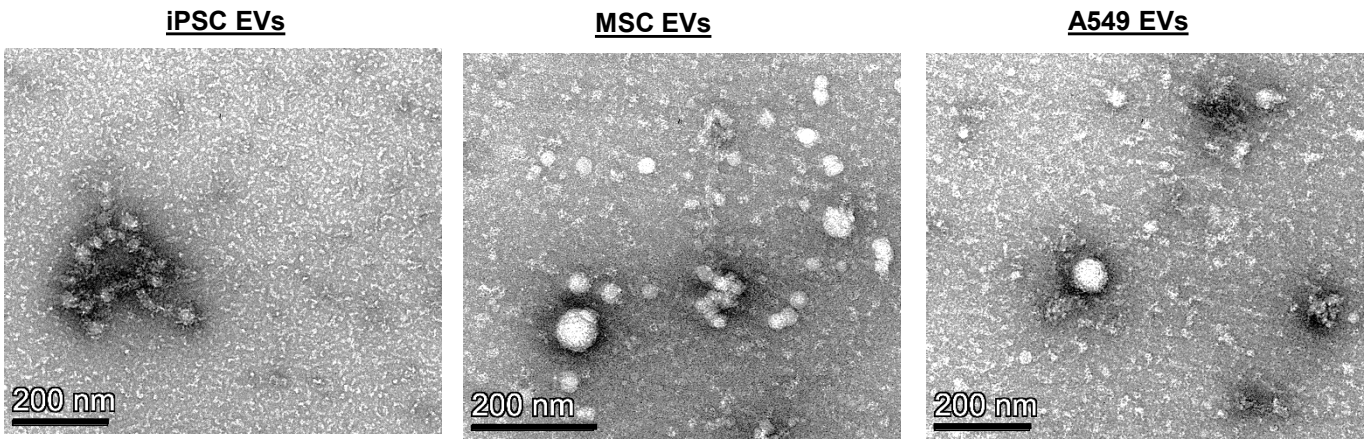

Branscome et al. Fig. 4a-b

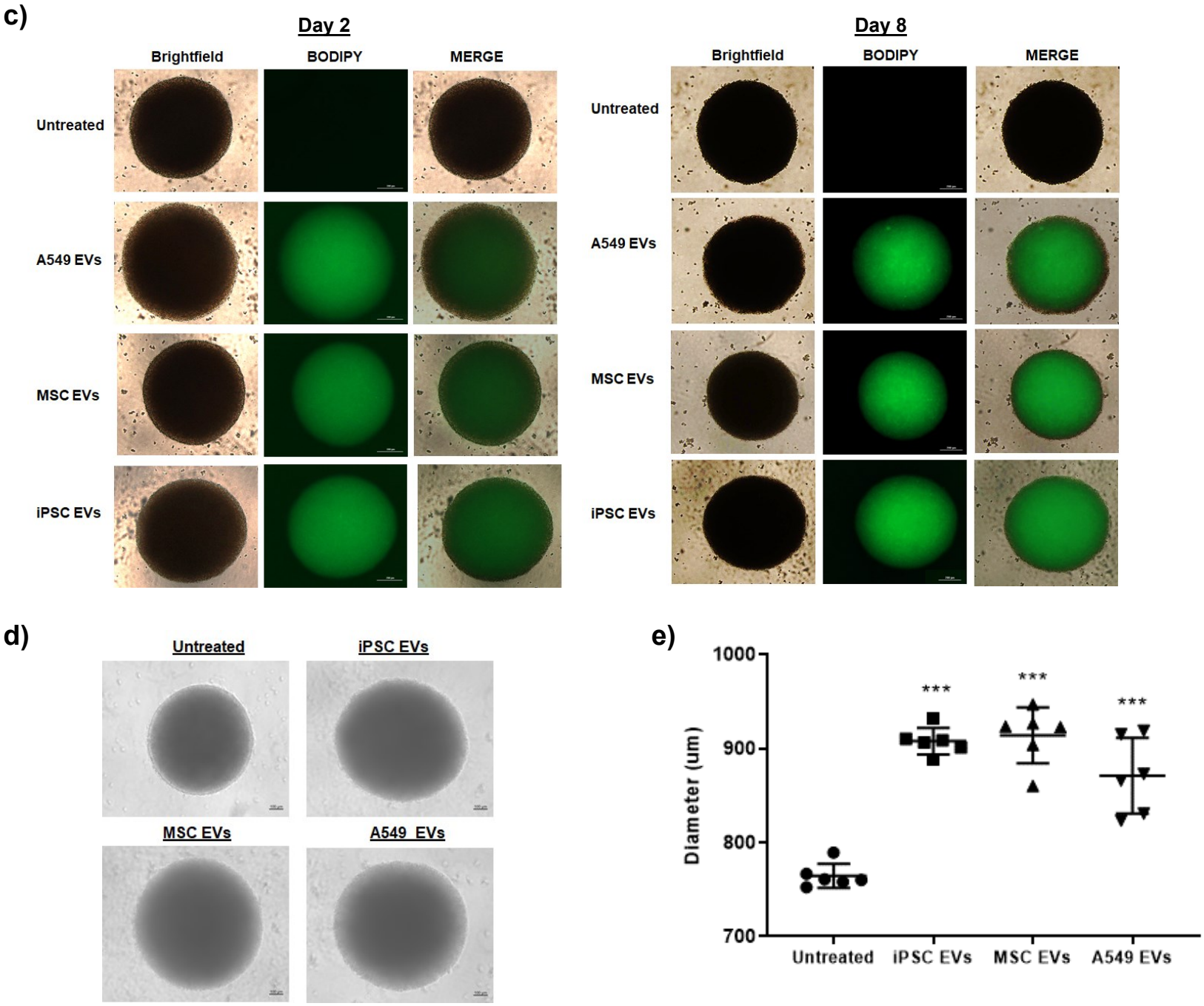

Branscome et al. Fig. 4c-e

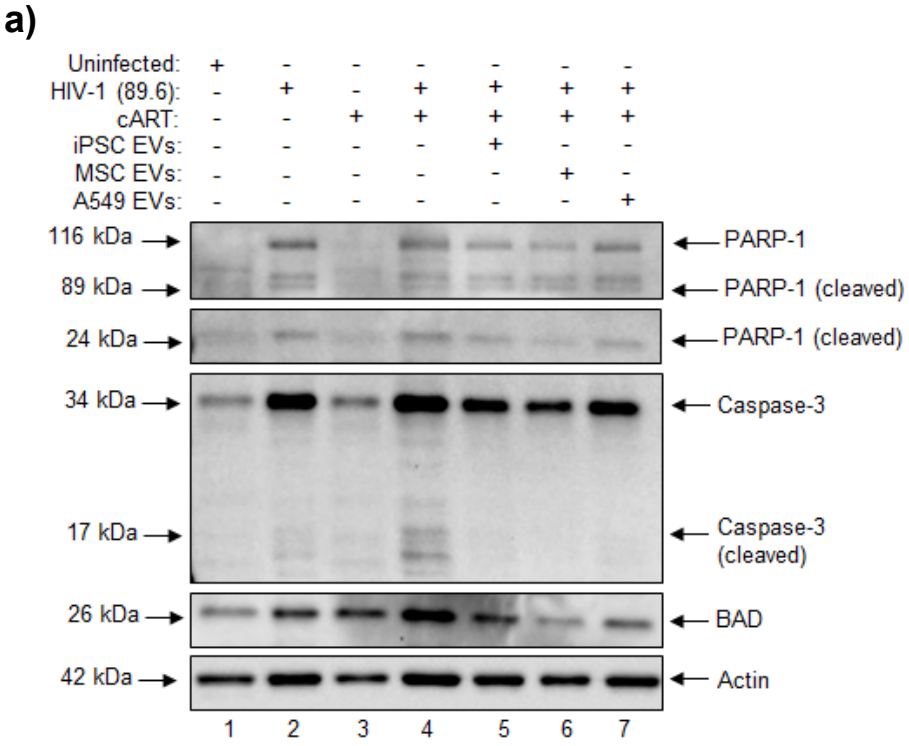

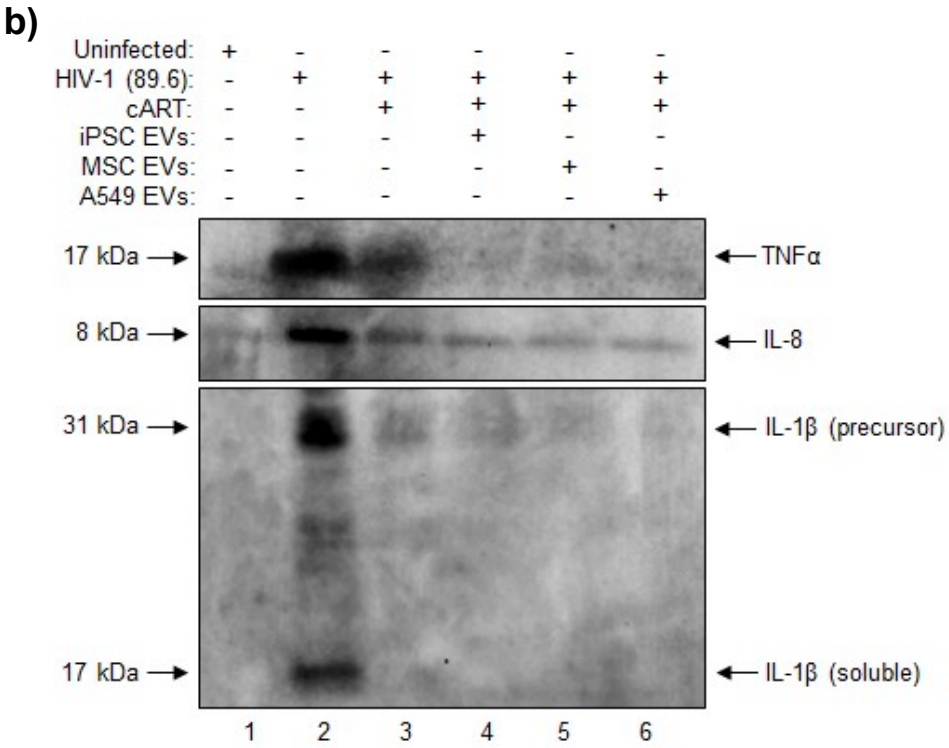

Branscome et al. Fig. 5a-b

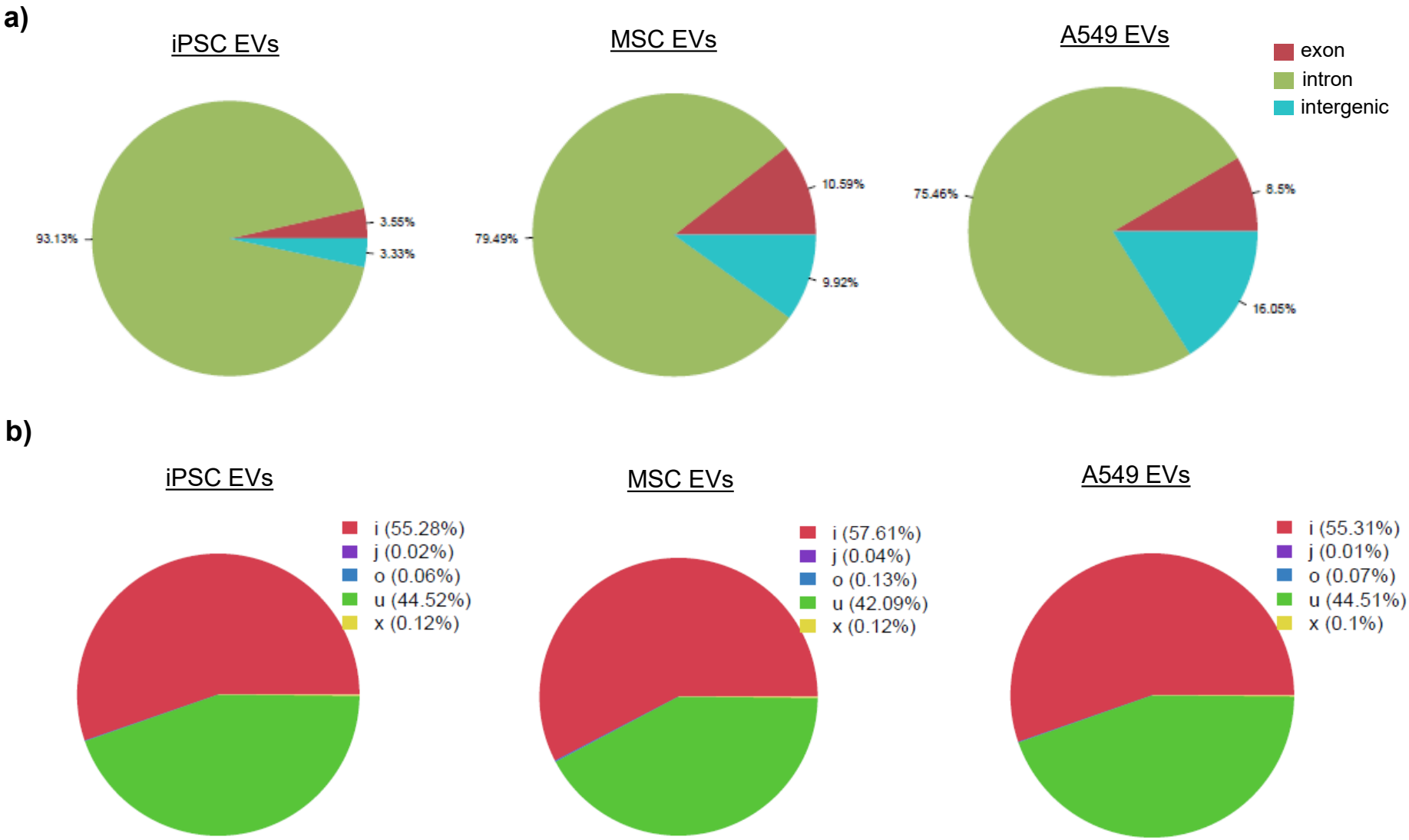

Branscome et al. Fig. 6a-b

c)

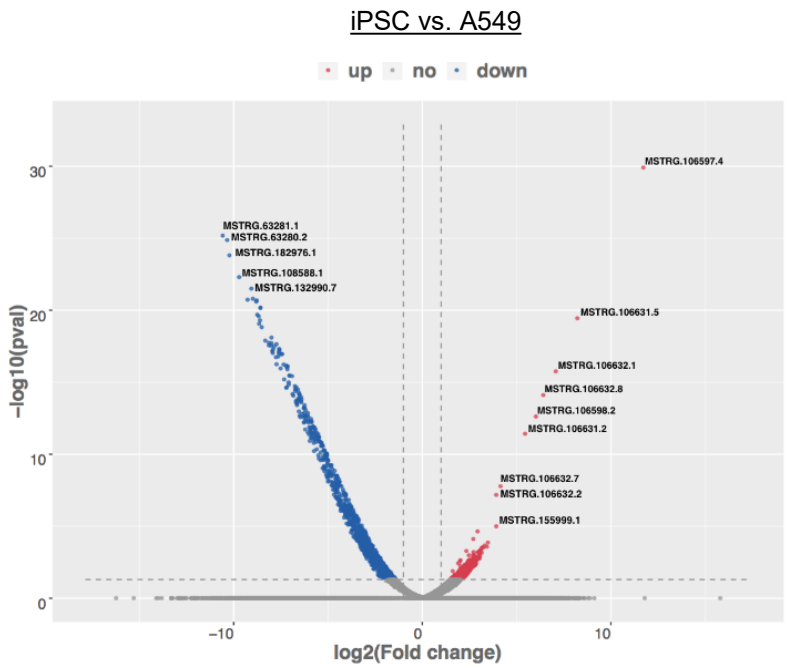

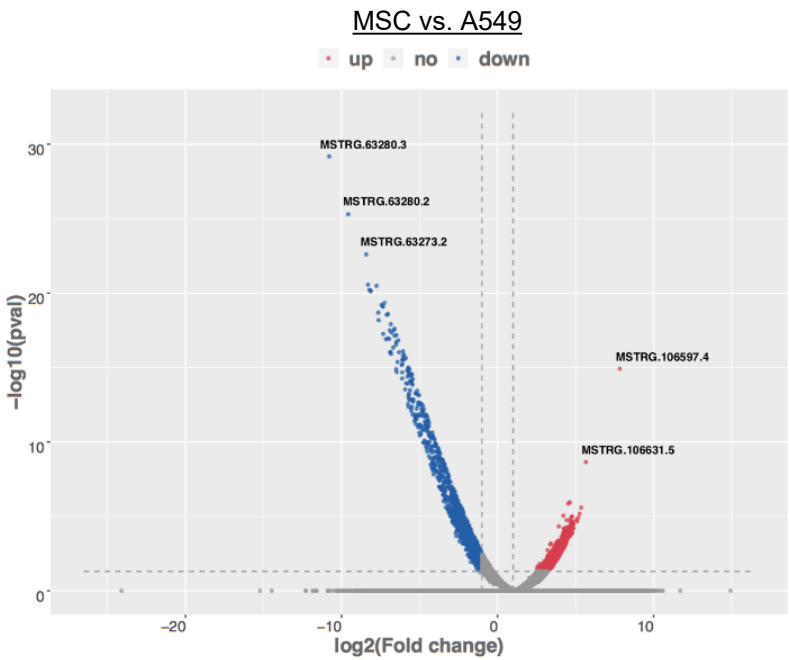

Branscome et al. Fig. 6c

a)

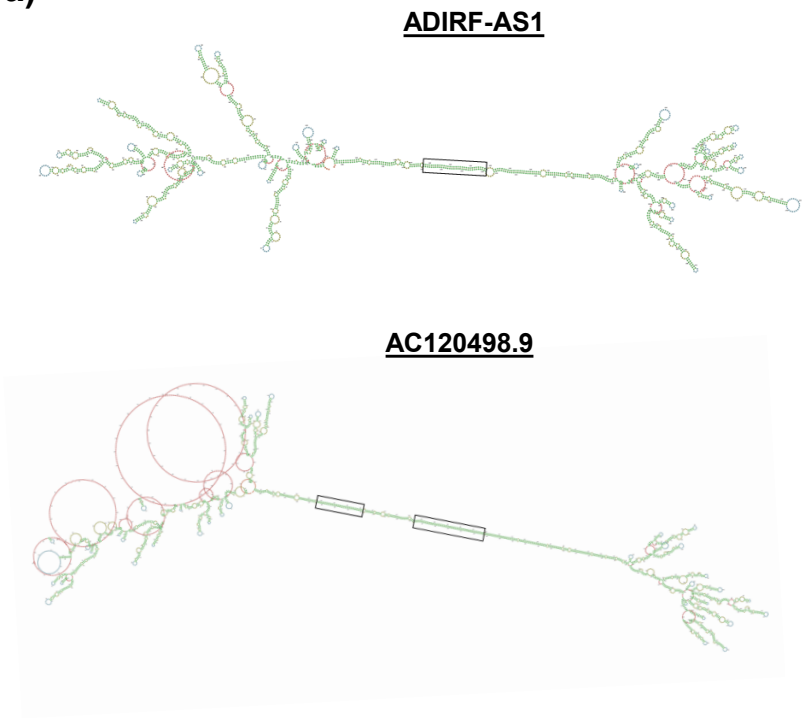

b)

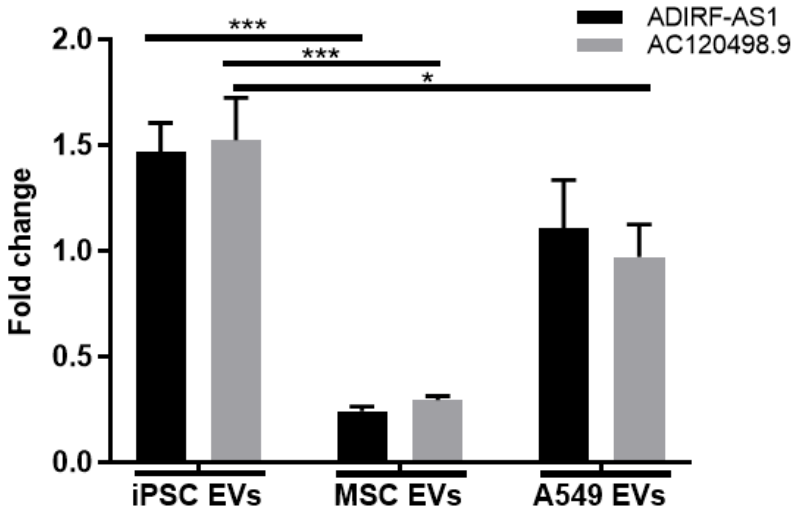

c)

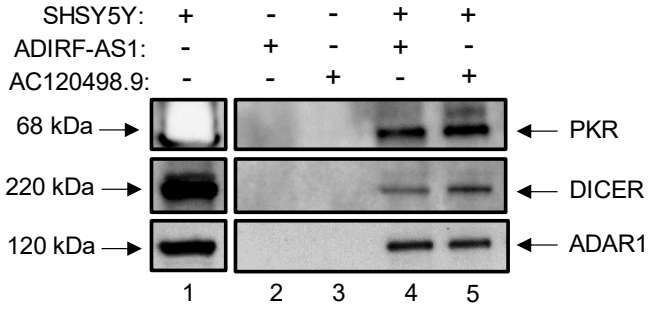

Branscome et al. Fig. 7a-c

d)

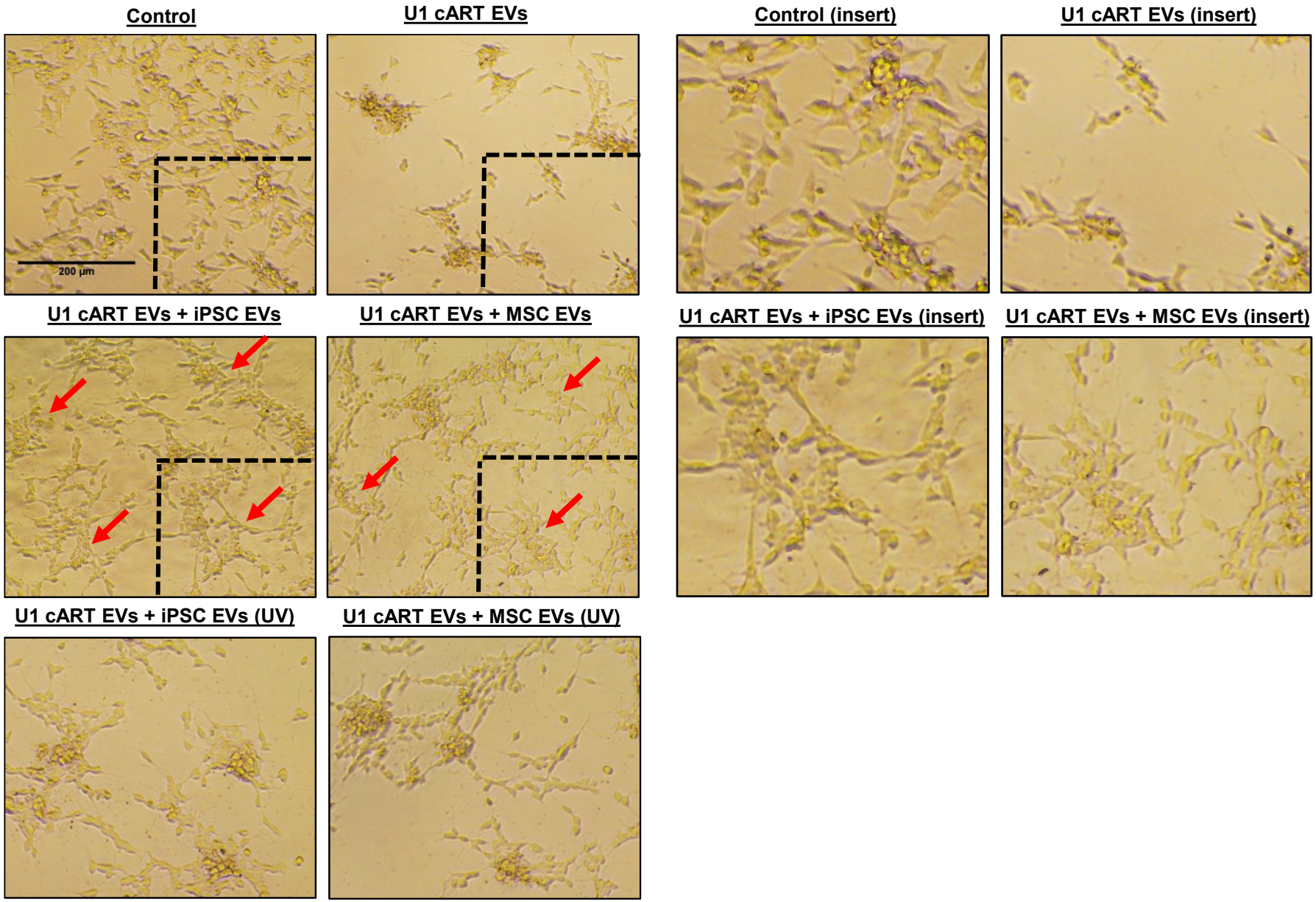

Branscome et al. Fig. 7d

e)

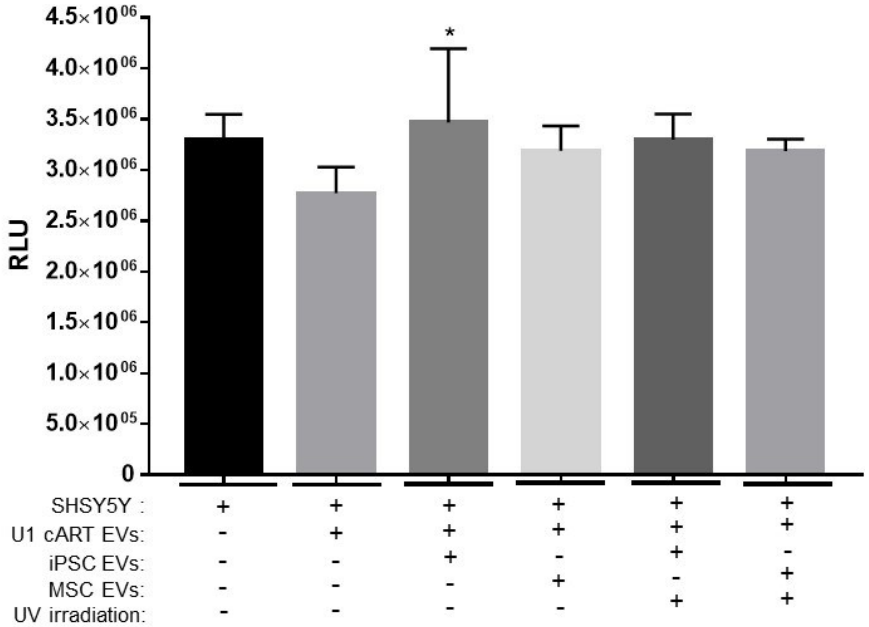

Branscome et al. Fig. 7e